Stem Cell Reports
Article

ISSCR

OPEN ACCESS

Engineering spatial-organized cardiac organoids for developmental toxicity testing

Plansky Hoang,[1,2] Andrew Kowalczewski,[1,2] Shiyang Sun,[1,2] Tackla S. Winston,[1,2] Adriana M. Archilla,[1,2] Stephanie M. Lemus,[1,2] A. Gulhan Ercan-Sencicek,[3] Abha R. Gupta,[4] Wenzhong Liu,[4] Maria I. Kontaridis,[3] Jeffrey D. Amack,[2,5] and Zhen Ma[1,2,*]

[1]Department of Biomedical and Chemical Engineering, Syracuse University, Syracuse, NY, USA
[2]BioInspired Syracuse Institute for Material and Living Systems, Syracuse, NY, USA
[3]Masonic Medical Research Institute, Utica, NY, USA
[4]Department of Pediatrics, Child Study Center, Yale School of Medicine, New Haven, CT, USA
[5]Department of Cell and Developmental Biology, State University of New York Upstate Medical University, Syracuse, NY, USA
*Correspondence: zma112@syr.edu
https://doi.org/10.1016/j.stemcr.2021.03.013

SUMMARY

Emerging technologies in stem cell engineering have produced sophisticated organoid platforms by controlling stem cell fate via biomaterial instructive cues. By micropatterning and differentiating human induced pluripotent stem cells (hiPSCs), we have engineered spatially organized cardiac organoids with contracting cardiomyocytes in the center surrounded by stromal cells distributed along the pattern perimeter. We investigated how geometric confinement directed the structural morphology and contractile functions of the cardiac organoids and tailored the pattern geometry to optimize organoid production. Using modern data-mining techniques, we found that pattern sizes significantly affected contraction functions, particularly in the parameters related to contraction duration and diastolic functions. We applied cardiac organoids generated from 600 μm diameter circles as a developmental toxicity screening assay and quantified the embryotoxic potential of nine pharmaceutical compounds. These cardiac organoids have potential use as an *in vitro* platform for studying organoid structure-function relationships, developmental processes, and drug-induced cardiac developmental toxicity.

INTRODUCTION

Recent progress in stem cell-based organoid technology offers unique opportunities to *in vitro* recapitulate biological processes of organogenesis into spatially organized tissue structures that resemble the architecture and functions of specific tissues (Fatehullah et al., 2016). Integration of organoid technology and microfabrication has provided promising ways to guide self-organization and spatial pattern formation of developing biological tissues (Brassard and Lutolf, 2019). For example, Microwell technology has been widely applied to control the aggregate sizes of human pluripotent stem cells (hPSCs) for generating brain (Lancaster et al., 2017), kidney (Czerniecki et al., 2018), and blastocyst (Rivron et al., 2018) organoids of a desired architecture. Microfluidic systems could precisely control the localization of morphogen source and gradient to guide spatial hPSC differentiation and organization into *in vitro* synthetic embryonic tissues, such as in germ layer patterning (Manfrin et al., 2019), as well as amniotic and epiblast layer separation (Zheng et al., 2019). Surface micropatterning techniques were also able to provide geometric confinement for modeling gastrulation, where patterned PSCs differentiated to form concentric rings indicative of specific germ layers (Morgani et al., 2018; Warmflash et al., 2014). These examples illustrate the critical need for spatiotemporal engineering of cell microenvironments to guide the structure and function of stem cell organoids to specific biological tissues.

Despite extensive efforts in controlling stem cell lineage specification via biophysical inputs, there are few studies focusing on how 2D patterned cell colonies could give rise to organoids with defined structure-function relationships. Understanding these relationships requires comprehensive analysis of multiple variables simultaneously, which increases the data dimensionality for analysis and visualization. As methods to detect tissue functions become more large scale and multidimensional, analysis requires more advanced analytics to effectively comprehend the functional outcomes. Data dimensionality reduction techniques, which are the basis of bioinformatics, are still underexplored for analyzing tissue-level structural and functional properties. The combination of tissue engineering, organoid technology, and advanced data-mining techniques would potentially provide the capability to discover trends and relationships to guide new engineering designs with a spectrum of biological structures and functions.

hPSC-derived organoids exhibit characteristics of specific tissue lineages at their early developmental stages, thus providing great potential as *in vitro* assays of developmental drug toxicity. *In vivo* animal models and *in vitro* mouse embryonic stem cell tests (mEST) are widely

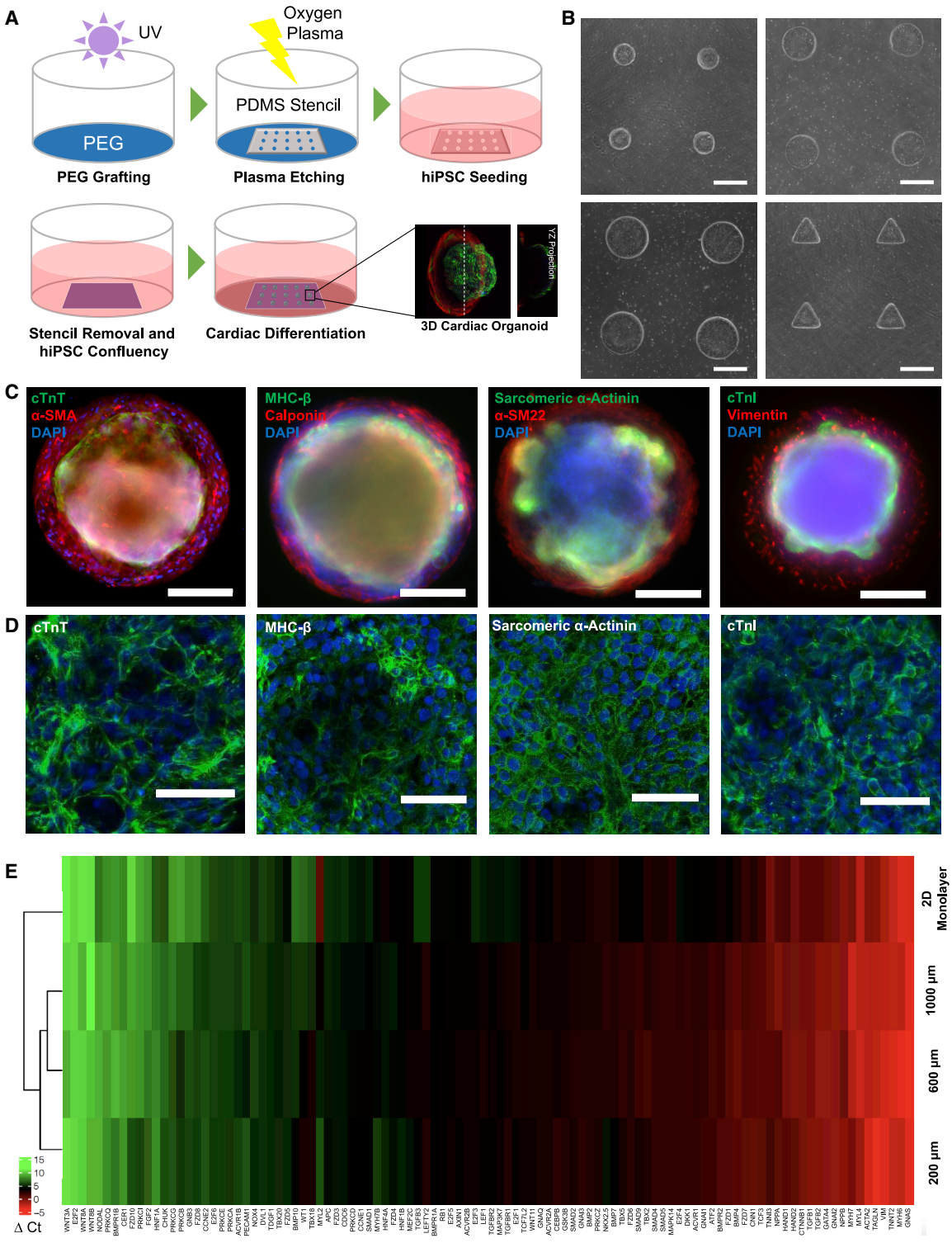

Figure 1. Human iPSC micropatterning and differentiation into cardiac organoids

(A) The procedure schematic for micropatterning hiPSCs on standard tissue culture plate using a selective PEG-based etching method.

(B) Bright-field microscopy images of arrays of micropatterned hiPSCs with different sizes and shapes. Scale bar, 400 μm.

(C) Spatial-organized cardiac organoids showed cardiac muscle on the top center with cardiomyocyte-specific proteins (cardiac troponin T [cTnT], β-myosin heavy chain [MHC-β], sarcomeric α-actinin, and cardiac troponin I [cTnI]) and smooth muscle-like cells on the perimeter

(legend continued on next page)

implemented by pharmaceutical companies as biological assays for embryotoxicity screening (Seiler and Spielmann, 2011). To overcome species barriers that impose limitations in traditional drug screening, hPSC technology has been proposed to replace the mEST for better predictions of human-specific developmental toxicity (Kumar et al., 2012). However, most 2D stem cell-based assays lack the capability of morphological scoring of 3D tissue morphogenesis. This undermines the predictability of drug-induced teratogenicity, which potentially manifests as structural malformations in prenatal development. Moreover, traditional organoid technology exhibits relatively random positioning of tissue regions of specific cell types, and these regions are not reliably spatially positioned relative to one another. Heterogeneity in organoid formation also makes it difficult for embryotoxicity drug testing purposes with high consistency and reproducibility. Advances in microtechnologies have produced organoids with consistent 3D morphology and spatial structure, enabling robust morphological scoring of *in vitro* tissue formation, which is crucial for screening drug-induced developmental toxicity.

In this work, we optimized cardiac organoid production from 2D micropatterned human induced PSCs (hiPSCs) by generating organoid arrays with different geometries (Hoang et al., 2018). Organoids generated from genome-engineered GCaMP6f hiPSCs were used for integrated functional analysis of calcium transient and contraction motion. Using data-mining tools, we established relationships among a multitude of organoid metrics of tissue structure and contractile functions. We also explored the inter-dependency among these parameters associated with the geometric sizes, which highlighted that biophysical microenvironment could modulate tissue structure and cardiac function. Next, we implemented this model for evaluating cardiac developmental toxicity by quantifying the drug effects based on cardiac differentiation, contractile behaviors and 3D tissue morphology. We also compared drug-induced cardiac developmental toxicity on hiPSC-based cardiac organoids to effects on *in vivo* cardiac development using whole embryo culture (WEC) of living *Danio rerio* (zebrafish) embryos. We envision the human cardiac organoid model as a versatile platform to assess cardiac organogenesis and developmental toxicity, which can be adopted for pharmaceutical development and fetal safety assessments.

RESULTS

Cardiac differentiation of patterned hiPSCs produces spatially organized cardiac organoids

Controlling biophysical microenvironments through cell-patterning techniques has been used for regulating stem cell differentiation and modeling mammalian embryonic development (Hwang et al., 2008; Ma et al., 2015; Shao et al., 2015; Warmflash et al., 2014). Geometric confinement to hiPSCs was provided by a poly(ethylene glycol) (PEG)-based micropatterned substrate created by oxygen plasma etching (Figure 1A). hiPSCs seeded on the micropatterned substrates (Figure 1B). Upon confluency, hiPSCs were differentiated via small-molecule modulation of the Wnt/β-catenin pathway (Figures S1A and S1B) (Lian et al., 2012). Patterned hiPSCs were able to proliferate, conform to the pattern geometry and retain pluripotency, as indicated by positive immunofluorescence of OCT4, NANOG, E-cadherin, SOX2, and SSEA4 (Figure S1C). This approach generated robust contracting cardiac organoids arrays of 50–100 organoids within 20 days.

At early differentiation stages, we verified positive expression of mesoderm marker BRA (day 1) (Figure S1D), and cardiac progenitor markers ISL1 (day 8), and NKX2.5 and GATA4 (day 10) (Figures S1E–S1G). Expression of early cardiac progenitor makers was distributed across the entire pattern before the cardiac organoids began contracting around day 12. As the contraction became robust over time, the cardiac tissue compacted toward the center, revealing the underneath stromal cells. At day 20 of differentiation, cardiomyocytes were primarily differentiated on the center top of the organoids, demonstrated by multiple cardiac-specific markers (Figures 1C and 1D): cardiac troponin T, myosin heavy chain β, sarcomeric α-actinin, and cardiac troponin I, while smooth muscle-like stromal cells along the pattern perimeter, indicated by positive expression of α-smooth muscle actin, calponin, α-SM22, and vimentin.

Next, we compared the gene expression profile between cardiac organoids from three different pattern sizes (200, 600, and 1,000 μm in diameter) and traditional 2D monolayer differentiation. In general, gene expression showed upregulation of cardiac-specific genes and downregulation of WNT signaling at day 20 differentiation, although the gene expression profile had closer similarity among different organoids than 2D differentiation (Figure 1E).

of the organoids with stromal cell markers (smooth muscle actin [α-SMA], calponin, transgelin [α-SM22]), and vimentin from 600 μm organoids. Scale bar, 200 μm.

(D) Maximum intensity confocal projections of cardiomyocytes on the cardiac organoids. Scale bar, 50 μm.

(E) Gene expression profile of cardiogenesis was compared between organoids of varying sizes with 2D monolayer differentiation. ΔCt values used in this gene map were calculated relative to the average Ct of GAPDH. HPRT1 and GUSB housekeeping controls.

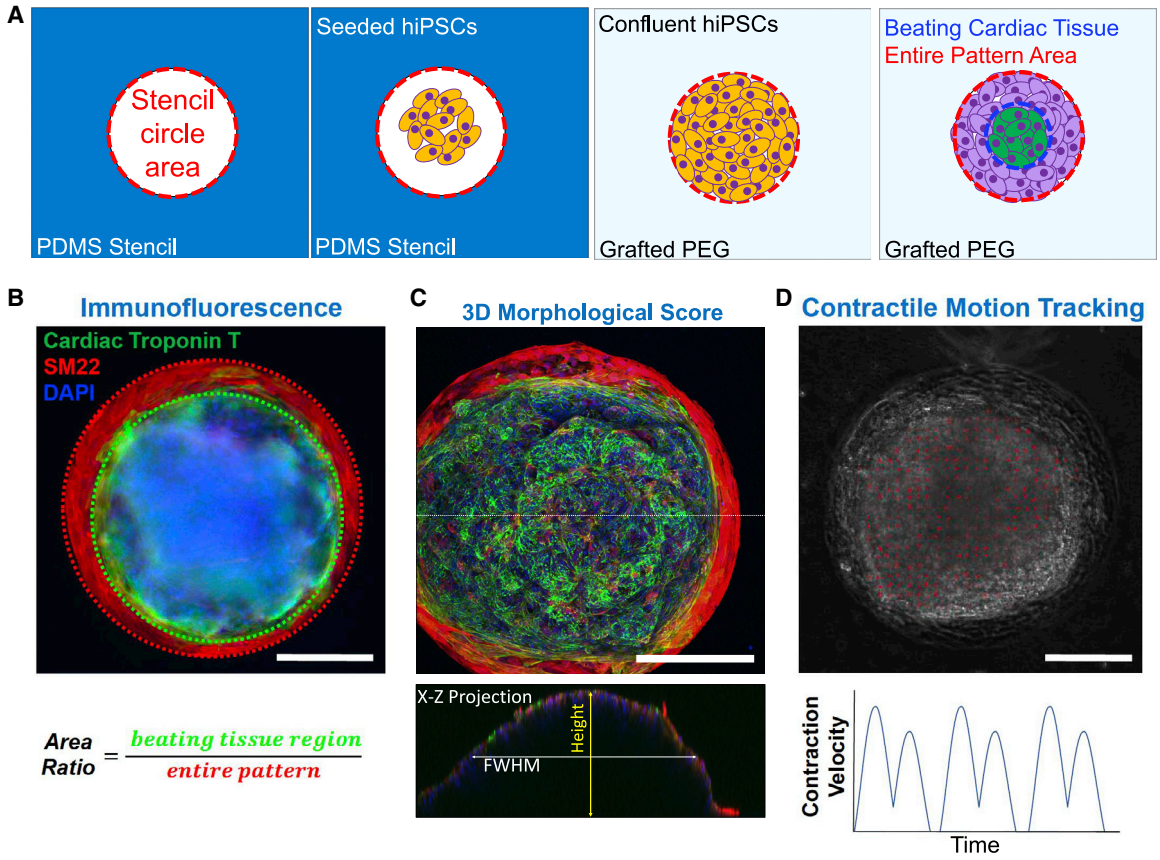

Figure 2. Cardiac organoid characterization metrics

(A) Schematic illustration of metrics used to calculate the area ratio. Red dotted outline illustrates the organoid area, which is equivalent to the stencil pattern area. Blue dotted outline illustrates the area of contracting cardiac tissue.

(B) Immunofluorescence staining used to compute the area ratio, which is the area of cardiac tissue (cTnT) coverage relative to the area of the entire pattern.

(C) Confocal imaging was used to capture z-stacks of the tissues, which were reconstructed for 3D morphological scoring of the height and full-width at half-maximum (FWHM).

(D) Motion tracking analysis based on vector computation of pixel movement generates contraction velocity waveforms representing beat cycles of the cardiac organoids. Graph shown represents a schematic illustration of contraction motion waveform and no data are associated. Scale bars, 200 μm.

The organoids also showed significantly higher gene expression related to transforming growth factor β (TGF-β) signaling (TGFB1, TGFB2, TGFB3, TGFBR1, and TGFBR1). This might relate to a high content of stromal cells in the organoids under geometric confinement on the patterned substrate (Figure S1H). To compare the organoids generated from different pattern sizes, we found that organoids of 600 and 1,000 μm showed upregulation of cardiac-specific genes (MYL4, MYH7, and NKX2.5), while smaller 200 μm organoids had higher expression of stromal cell genes (ACTA2, TAGLN, and VIM). These results illustrated that high geometric confinement from smaller patterns promoted the differentiation into supportive cell types.

Pattern geometry dictates structural morphology and contractile physiology of cardiac organoids

Using immunofluorescence staining, we measured the cardiac tissue distribution by calculating the *area ratio* between the areas of cardiomyocyte differentiation and entire pattern area (Figures 2A and 2B). Using confocal microscopy and 3D image reconstruction (Videos S1 and S2), we assessed the three-dimensionality of cardiac organoids by measuring the height and full-width at half-maximum (FWHM) (Figure 2C). To study the contractile functions of cardiac organoids, we generated the cardiac organoids from genome-edited hiPSC line with GCaMP6f reporter (Chen et al., 2013; Huebsch et al., 2016; Mandegar et al., 2016), which provided us

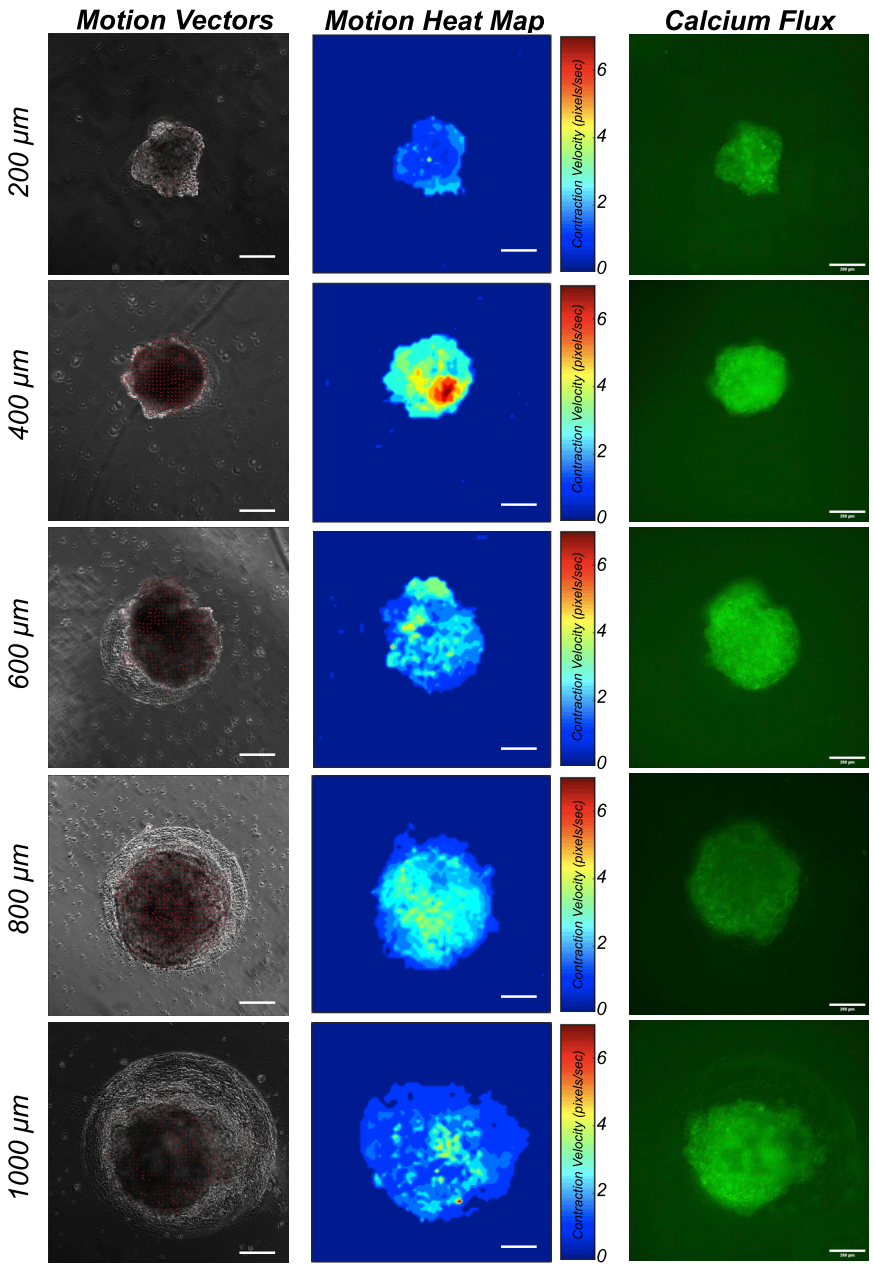

Figure 3. Contraction functions of cardiac organoids ranging in size from 200 μm (top) to 1,000 μm (bottom) in diameter

Contraction functions were assessed using contraction motion tracking (left), which computes contraction magnitude as a function of the contraction velocity (middle). Fluorescent calcium flux (right) was measured to further characterize contraction behavior by classifying the calcium handling properties. Scale bars, 200 μm.

the capability to assess the cardiac contractions using bright-field motion tracking analysis (Huebsch et al., 2015) (Figure 2D; Video S3). Motion data were integrated with fluorescent calcium flux (Figures S2A and S2B; Video S4) for a comprehensive characterization of contraction functions. t-SNE plots, together with a heatmap, were generated using quantified contractile function parameters from individual organoids with different pattern sizes: *area ratio* between GCaMP6 fluorescence and pattern area, *beat rate*, *maximum calcium flux*, *pulse duration* of calcium flux cycle (τ_0, τ_{50}, and τ_{75}), *peak-to-peak interval*, *maximum contraction velocities*, and *relaxation velocities* (Figure S2C).

To examine the effects of pattern size on cardiac organoid development, we generated organoids from circular patterns ranging from 200 to 1,000 μm in diameter (Figures 3 and 4A). The 200 μm patterns did not reliably produce the organoids with a relatively low organoid production efficiency (~20%), in comparison with all other sizes (~80%). Albeit with the largest variability, 200 μm circle patterns produced the cardiac organoids with the largest area ratio of cardiac muscles among all the sizes (Figure 4B).

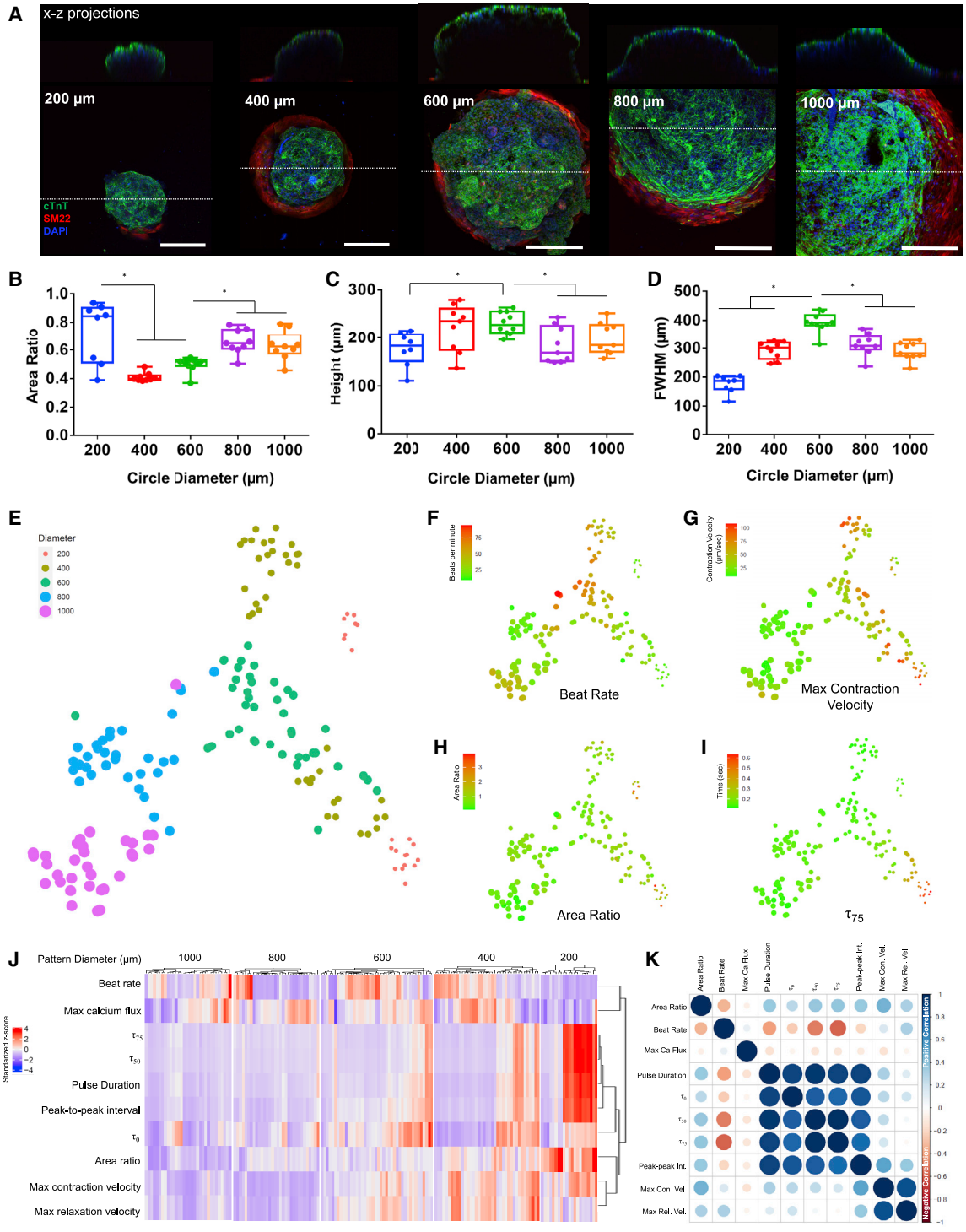

Figure 4. Pattern size effects on cardiac organoid characteristics

(A) Cardiac organoids generated from the circular patterns with different sizes (200–1,000 μm in diameter) showed spatial-organization of cardiomyocytes and stromal cells and 3D dome shape in the X-Z plane. Scale bar, 200 μm.

(B–D) (B) The area ratio between cardiomyocyte staining and entire pattern size showed larger coverage but higher variation in cardiac muscle differentiation on the cardiac organoids of 200, 800, and 1,000 μm patterns (n = 9, *p ≤ 0.0001 between 200 and 400/600 μm; *p ≤ 0.0001 between 400/600 and 800/1,000 μm). The cardiac organoids of 600 μm patterns exhibited better 3D morphology with largest

(legend continued on next page)

Regarding large sizes (800 and 1,000 μm in diameter), these patterns produced the organoids with a greater area ratio, but lower organoid height than the ones from 400 to 600 μm circles (Figure 4C). In addition, the FWHM steadily increased with increasing pattern size, peaked at 600 μm patterns, and decreased at larger sizes (Figure 4D). This indicated that 600 μm patterns produced the cardiac organoids with high consistency and large 3D morphology.

From the t-SNE plot (Figure 4E) generated from data mining of contraction function parameters (Figure S2C), organoids of larger sizes (600, 800, and 1,000 μm) were better clustered with high consistency. Organoids from 200 to 400 μm patterns showed significant organoid divergence with separated clusters, indicating less consistency in organoid properties. We also used t-SNE plots to illustrate the gradients of each parameter across the organoid sample distribution (Figures 4F–4I and S3A–S3F). Organoids of larger patterns exhibited higher beat rate (Figure 4F), while smaller patterns exhibited higher contraction and relaxation velocities (Figures 4G and S3A). Consistent with the confocal structural analysis, the 200 μm organoids produced the largest area ratio of cardiac tissue relative to pattern size (Figure 4H). In these t-SNE plots, the divergence of small organoids from 200 to 400 μm pattern primarily resulted from the significant differences on parameters of contraction duration (peak-to-peak intervals, pulse duration, τ_{50}, τ_{75}) (Figures 4I and S3B–S3D). The metrics of τ_0 and maximum calcium flux exhibited no apparent trends among different organoid sizes (Figures S3E and S3F).

These parameters for the cardiac organoids of different sizes were then compared in a heatmap (Figure 4J). Organoids larger than 200 μm exhibited comparable trends of beat rate and maximum calcium flux, indicating efficient calcium handling and consistent beat frequency. Meanwhile, the contraction duration parameters of peak-to-peak intervals, pulse duration, τ_{50}, and τ_{75} showed high levels of size dependency. The prolongation of contraction duration, especially regarding calcium decay in the cardiac organoids from small patterns, is prone to arrhythmia related to the abnormal diastolic functions (Periasamy and Janssen, 2008; Weber et al., 2006). From the correlation matrix (Figure 4K), strongest correlations were observed between parameters of calcium analysis (τ_0, τ_{50}, τ_{75}, pulse duration), which had negative correlation with beat rate (Figures S3G and S3H). Furthermore, there was a strong positive correlation between calcium decay from calcium flux analysis and peak-to-peak interval from contractile motion analysis. More importantly, area ratio from morphological analysis is positively correlated with calcium decay and contractile motion velocities from different functional analysis, indicating a structure-function relationship between the relative tissue size and cardiac contraction cycles.

In addition, we compared circle, square, and triangle organoids with the same area (Figure 5A). Cardiac organoids from circular patterns exhibited significantly higher contraction velocity, lower beat rate, and longer beat duration (Figures 5B–5D). Furthermore, circle patterns produced the organoids with larger area ratio, height, and FWHM than squares and triangles (Figures 5E–5G). Overall, the circular pattern geometry promoted more robust formation of cardiac organoids with large size and high contractile functions. These observations illustrated that the development of cardiac organoids was affected by pattern shape, in which the angular geometries presented high physical constraint to the cells and promoted a higher degree of differentiation into the stromal cell types, rather than cardiomyocytes. By plotting the structure-function correlations and structure-structure correlations, we observed a decline in the beat rate that corresponded to the increasing area ratio (Figures 5H and 5I) as a negative correlation between the cardiac tissue size and the beat rate.

Cardiac organoids as an *in vitro* assay for cardiac developmental toxicity

The heart is the first functional organ to form, thus cardiac differentiation is often used as a key evaluation for developmental toxicity (Tandon and Jyoti, 2012). Since 600 μm diameter circular patterns gave robust organoid production, large 3D morphology, consistent contractile functions, and high level of cardiac-specific differentiation,

values in (C) height (n = 8, *p = 0.0126 between 200 and 600 μm; *p = 0.0126 between 600 and 800/1,000 μm) and (D) FWHM (n = 8, *p $\leq$ 0.0001 between 600 and 200/400 μm; *p $\leq$ 0.0001 between 600 and 800/1,000 μm).

(E–I) (E) Contractile function parameters were used to cluster individual organoids with different pattern sizes and generate a t-SNE plot to evaluate organoid-to-organoid correlations. t-SNE gradients were plotted for (F) beat rate, (G) maximum contraction velocity, (H) τ_{75}, and (I) area ratio.

(J) Heatmap illustrating all contractile functions parameters relative to pattern size showed strong correlation between size and prolonged contraction duration, especially for the organoids of small patterns.

(K) Correlation plot illustrated proportional relationships between contraction duration parameters, but inverse correlations between contraction duration and contraction rate. All boxplots show the minimum, maximum, median, and 25th and 75th percentiles, and statistical analysis was performed based on analysis of variance (ANOVA) with Tukey's multiple comparison test. Data were pooled from three independent experiments.

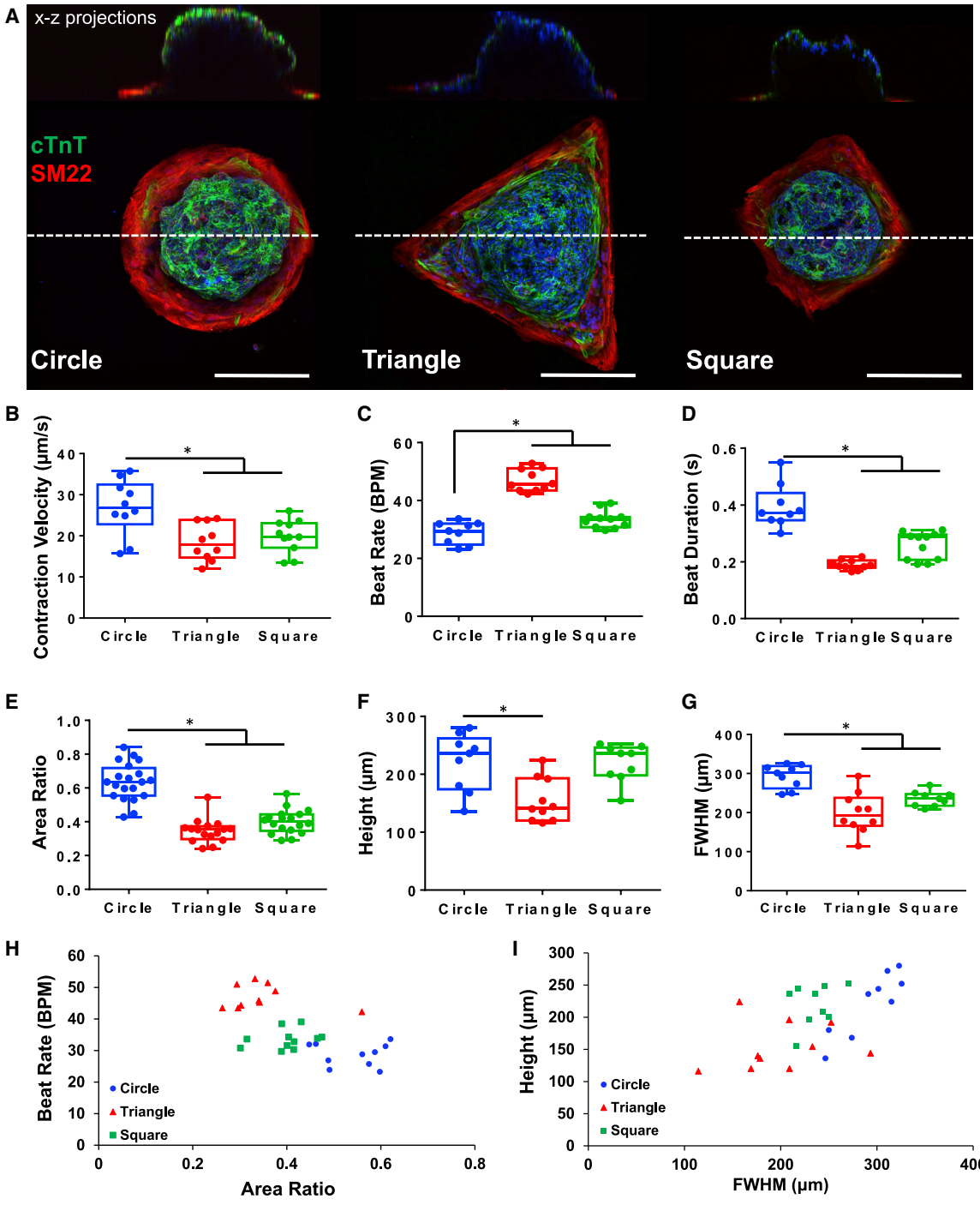

Figure 5. Polygonal geometry effects on cardiac organoid development

(A–D) (A) Z-Projection of confocal images of cardiac organoids generated in circular, triangular, and square shapes. Scale bars, 200 μm. Triangular and square organoids exhibited (B) significantly decreased contraction velocity ($n \geq 10$, *p = 0.0024), but (C) significantly faster beat rate ($n \geq 9$, *$p \leq 0.0001$), and (D) longer beat duration ($n \geq 9$, *$p \leq 0.0001$) relative to circular organoids.

(E) Morphological scoring of cardiac organoids showed that circle shapes produced organoids that were significantly larger in area ratio ($n \geq 16$, *$p \leq 0.0001$) than triangle and square organoids.

(F and G) (F) Only triangle organoids produced significantly decreased tissue height ($n \geq 9$, *p = 0.0013), (G) while both triangular and square organoids had significantly smaller FWHM ($n \geq 9$, *$p \leq 0.0001$).

(legend continued on next page)

arrays of cardiac organoids from this geometry were used to test the capabilities of this platform to be implemented as a cardiac developmental toxicity assay. Using flow cytometry, we quantified the consistency of cardiac differentiation efficiency of organoids and 2D monolayer differentiation from five different batches (n = 5) across ten passages of hiPSCs from two different lines. Both organoids of 600 μm and 2D differentiation produced over 50% cells that were positive for cardiac troponin T (Figures 6A and 6B). These results illustrated that cardiac organoids can be generated consistently across multiple cell batches and multiple hiPSC lines. Furthermore, the result of ~50% cTnT+ cells from flow cytometry was consistent with the area ratio calculation, where 600 μm organoids exhibited an average area ratio of approximately 0.5 (Figure 4B). Since the percentage of cTnT+ cells that composed organoids was comparable with the area ratio metric, we inferred that the area ratio is an appropriate metric to approximate cardiac differentiation efficiency for the drug-screening purposes.

Nine drugs (Table S1) used in this study covered the entire spectrum of the past FDA pregnancy category system that ranked drugs from A (safe) to X (toxic) based on predicted teratogenic risk. First, we compared two drugs between category A (doxylamine succinate) and category X (thalidomide). The cardiac differentiation efficiency remained consistent for doxylamine succinate treatment, whereas thalidomide resulted in a clear decrease in cardiac differentiation with each increasing dose (Figure 6C). Next we performed a more comprehensive embryotoxicity assessment characterizing differentiation (area ratio), 3D tissue morphology, and contraction functions (Figure 7A). Doxylamine succinate (category A, Figure 7B) treatment had no negative effects on cardiac area ratio, whereas thalidomide (category X, Figure 7C) had produced the abnormal cardiac organoids with less cardiac tissue relative to the untreated controls (Figures 7D and 7E). Doxylamine succinate had prominent effects on the contractile functions with lower contraction velocity and slower beat rate (Figures 7F and 7H) due to its anticholinergic effects as an H1 receptor antagonist. Generally used as a sleeping aid, doxylamine succinate is also prescribed as an analgesic to reduce muscle tension. It is possible that the reduction of muscle contraction due to doxylamine treatment led to less tissue compaction, which resulted in an increase of area ratio. In contrast, there was no significant effect from thalidomide on contraction velocity (Figure 7G), although high dosage led to high variability in the beat rate (Figure 7I). More importantly, high concentration of thalidomide (100 μM) impaired the 3D morphology of the cardiac organoids with significantly lower height and FWHM relative to organoids treated with doxylamine succinate (Figure 7J) and to the controls (Figures 7K–7M). The impairment of cardiac tissue is potentially caused by fibroblast growth factor antagonism of this drug, resulting in decreased muscle development. These results indicated that exposure of a well-known teratogen resulted in severe impairment to hiPSC differentiation and organization into 3D cardiac organoids, which confirmed that this organoid model was sensitive to morphological defects as a result of drug exposure.

Three antibiotic drugs tested on the cardiac organoids showed increased developmental toxicity with the increase of their risk classification in the pregnancy category. Amoxicillin (category B antibiotic) in mammalian cells has been shown to induce DNA lesions as a result of amoxicillin-induced oxidative stress (Li et al., 2007). Amoxicillin showed no clear toxic effect on either structure or functions of the cardiac organoids at all three tested concentrations (Figure S4A). Rifampicin (category C antibiotic) targeting bacterial RNA and DNA for its effectiveness, has been shown to inhibit protein synthesis in mammalian cells (Buss et al., 1978). Rifampicin showed severe developmental toxicity at a high concentration (100 μM) with no organoid formation (Figure S4B). Doxycycline (category D antibiotics) inhibits the synthesis of bacterial proteins by binding to the 30S ribosomal subunit, but also showed adverse effects on mitochondrial ribosomes within mammalian cells (Ahler et al., 2013). Doxycycline treatment resulted in severe impairment on cardiac differentiation and organoid formation even at a moderate concentration (10 μM) (Figure S5A).

We then tested other category D dugs with various therapeutic applications. Lithium carbonate (category D antidepressant), which inhibits the PKC signaling for its psychiatric medication purpose, appeared to inhibit phosphatidylinositol cycle and Wnt pathway activation, based on mEST assays (Shaikh Qureshi et al., 2014). Exposure of lithium did not affect the contractile functions of the cardiac organoids but exhibited mild toxicity to the organoid formation measured by area ratio and FWHM (Figure S5B). Phenytoin (category D anticonvulsant) protects against seizures via voltage-dependent antagonism of voltage-gated sodium channels. Phenytoin exposure produced smaller cardiac organoids than controls, but still maintained

(H) Structure-function correlation plot illustrate that area ratio is negatively correlated to beat rate for these three geometric shapes. (I) Structure-structure correlation plot illustrate that organoid structure is also strongly correlated with geometry where circular organoids had the largest 3D structures. In all panels, boxplots show the minimum, maximum, median, and 25th and 75th percentiles, and statistical ANOVA with Tukey's multiple comparison test. Data were pooled from three independent experiments.

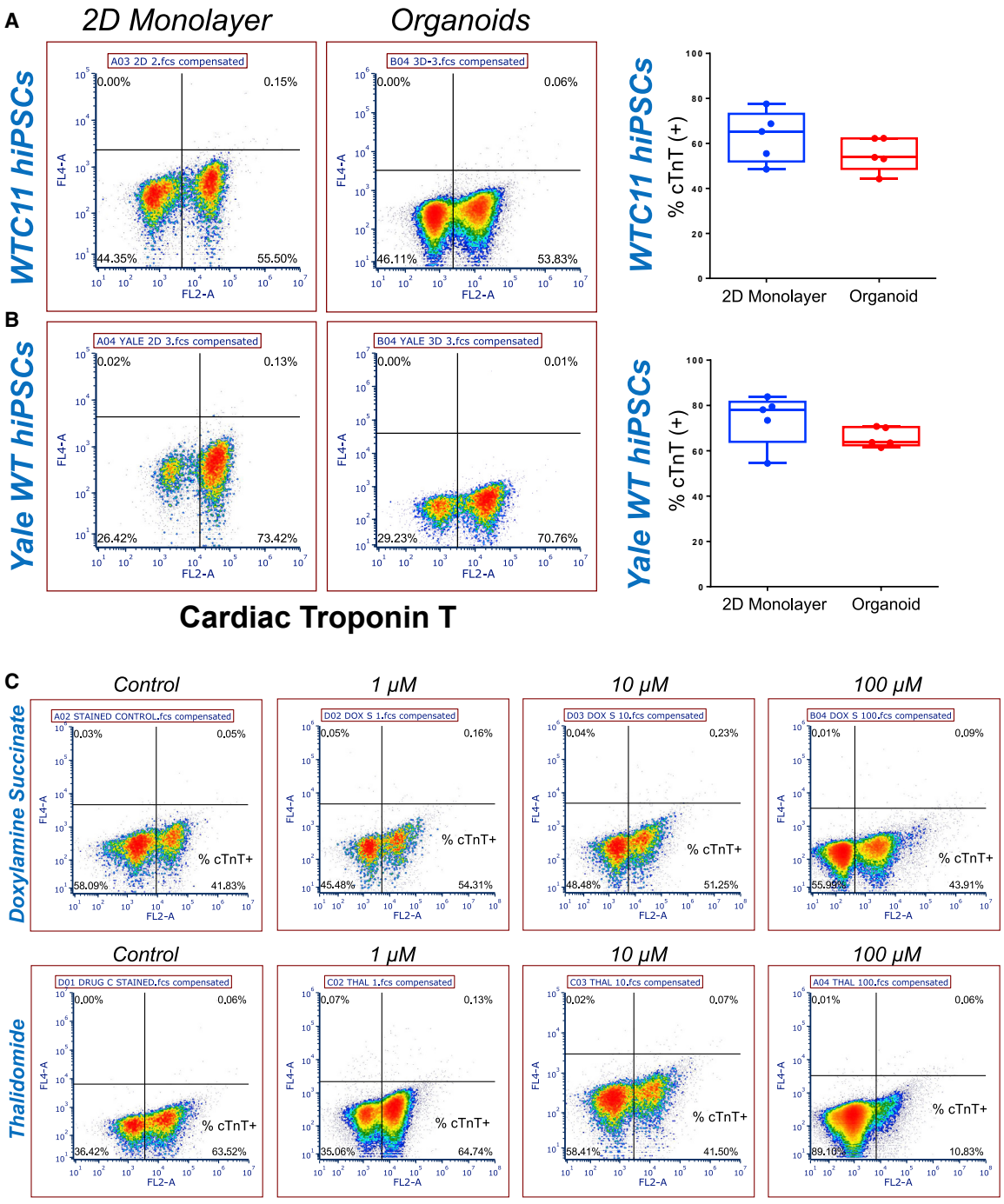

Figure 6. Flow cytometry quantification of cardiac differentiation efficiency

(A) 2D monolayer differentiation and organoid differentiation using WTC11 hiPSCs show that over 50% cells are cTnT+ cardiomyocytes.

(B) Reproducibility was demonstrated using a second hiPSC line (Yale WT), which also resulted in over 50% of cells expressing cTnT. Sample size n = 5.

(C) Flow cytometry density plots quantifying cardiac differentiation efficiency of organoids treated with doxylamine succinate and thalidomide. Doxylamine succinate treatment concentrations did not affect the percentage of cells expressing cTnT. Thalidomide treatment caused a considerable reduction in cTnT+ cells with increasing concentration. Data were pooled from at least three independent experiments.

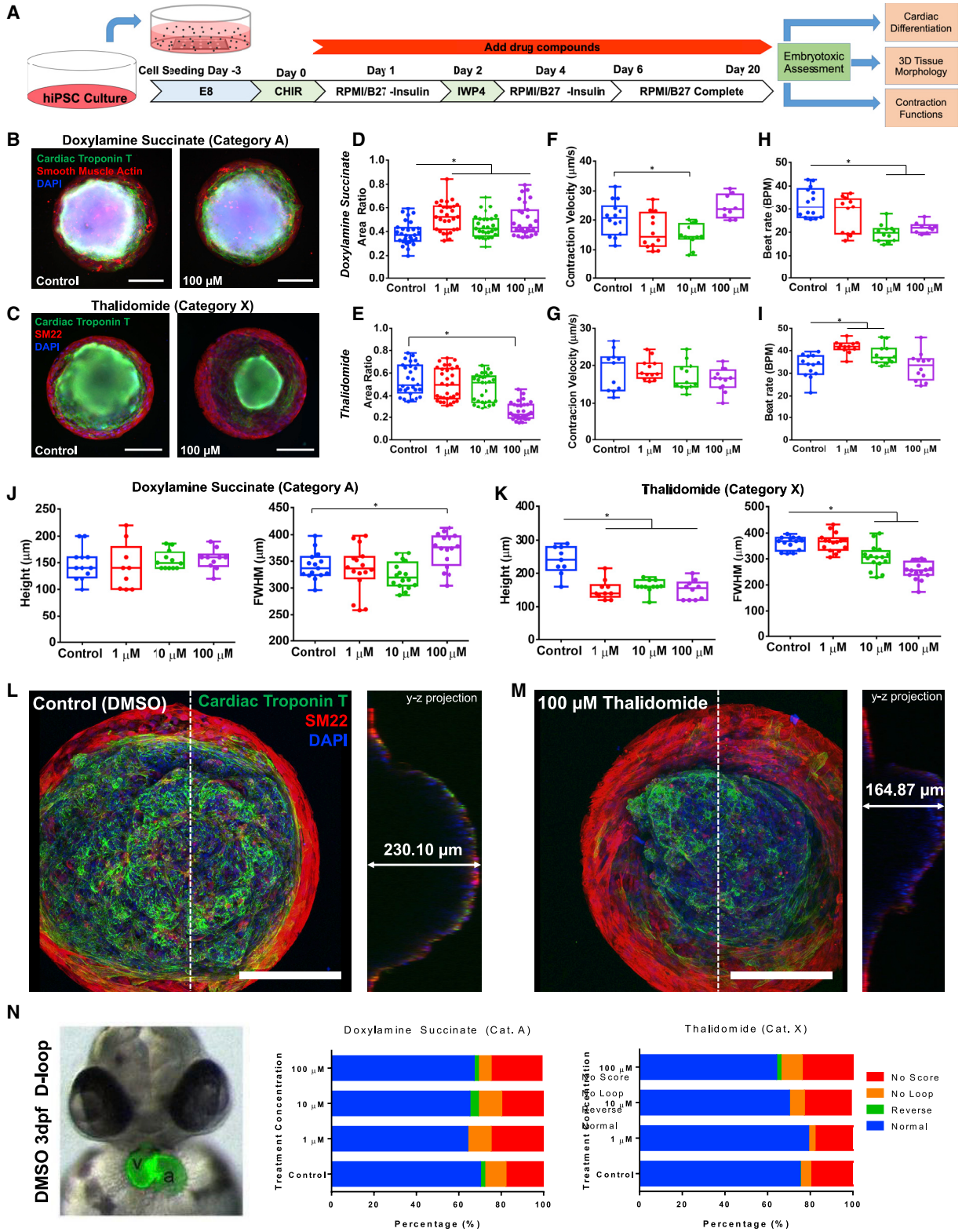

Figure 7. Cardiac organoids as a developmental toxicity screening assay

(A–H) (A) The timeline of cardiac organoid generation and continuous drug exposure. Epi-fluorescent microscopy images of the cardiac organoids for comparison between untreated controls with (B) doxylamine succinate (category A drug) and (C) thalidomide (category X

(legend continued on next page)

structural integrity (Figure S5C). Due to its inhibition on sodium channels, the cardiac organoids stopped beating at a high concentration (100 μM), until the drug was removed to allow the organoids to recover the contractile functions. Tretinoin (all-*trans*-retinoic acid, category D retinoid) treatment completely abolished the cardiac differentiation at a concentration as low as 10 μM, but still produced the organoids with comparable height and overall size as controls (Figure S6A).

Overexposure to retinoids was shown to result in birth defects from retinoic acid deficiency with decreased levels of retinoic acid-producing enzymes (Lee et al., 2012). Hence, we also tested isotretinoin (13-*cis*-retinoic acid, category X retinoid) (Figures S6B and S6C) on the cardiac organoids. Similar to tretinoin, isotretinoin produced large organoids at all tested concentrations, but totally abolished the cardiac differentiation at even lower concentration at 1 μM. This implied that retinoids caused severe impairment to the cardiac differentiation, but not tissue growth. Overall, these results verified that this cardiac organoid model was sensitive to the drug-induced cardiac developmental toxicity and offered the capability of morphological scoring based on the 3D tissue formation, which is often not available from other stem cell-based *in vitro* assays.

Last, we compared the developmental toxicity of these drugs between the cardiac organoid model and zebrafish whole embryo culture (zWEC), a well-established toxicity assay with promising potential to screen for teratogenicity (Lantz-McPeak et al., 2015). We used transgenic *Tg*(*myl7*:*GFP*) (Huang et al., 2003) with GFP only in cardiomyocytes, which allowed us to readily score myocardial development and heart tube looping at 48 h post fertilization (Sarmah and Marrs, 2016) (Figures 7N and S7A). Live zebrafish embryos were collected and exposed to the identical drugs and concentrations used in the cardiac organoid assay. Consistent with the organoid model, exposure with doxylamine succinate (category A) had negligible effect on the zebrafish embryonic heart development, as there was a considerable proportion of embryos exhibiting normal D-looped heart across all concentrations. However, the effects of thalidomide on zebrafish embryonic heart development were not as significant as we observed in the organoid model. We found that the proportion of normal heart looping did not notably decrease at higher concentrations of thalidomide (Figure 7N). Rifampicin (Figure S7C) and phenytoin (Figure S7B) showed mild embryotoxic effects to the zebrafish embryos at the highest concentration, while amoxicillin (Figure S7D), lithium carbonate (Figure S7E), and doxycycline (Figure S7F) showed moderate toxicity. Retinoids, tretinoin (Figure S7G), and isotretinoin (Figure S7H), at low concentration (0.1 μM), resulted in embryos with smaller heart size and abnormal morphology. At higher concentrations, the hearts failed to develop, as indicated by 0% of embryos expressing the GFP transgene. Upon comparing the organoid model with the zWEC model, we saw developmental toxicity that was comparable for between these two systems for most of drugs (doxylamine succinate, amoxicillin, lithium carbonate, phenytoin, tretinoin, and isotretinoin). However, rifampicin, doxycycline, and thalidomide showed distinct mismatch between these two model systems. We infer that this might be due to a number of factors, including species differences, method of drug exposure, and differences in the range of effective treatment concentrations.

DISCUSSION

The majority of *in vitro* cardiac tissue models focus on accurate recapitulation of physiologically relevant tissue structures of adult human heart, which are generally achieved by populating pre-fabricated 3D biomaterial scaffolds with pre-differentiated hiPSC-derived cardiomyocytes (hiPSC-CMs) (Ogle et al., 2016; Rodrigues et al., 2018;

drug). The area ratio of cardiac muscle coverage showed (D) an increase with doxylamine succinate ($n = 29$, $^*p \leq 0.0001$), but a decrease with thalidomide at high concentration ($n \geq 28$, $^*p \leq 0.0001$). The contraction velocity of cardiac contractile motion showed no drug effect from (F) either doxylamine succinate (G) or thalidomide. The beat rate showed (H) a decrease with doxylamine succinate ($n \geq 9$, $^*p \leq 0.0001$), and an increase with thalidomide at 1 and 10 μM concentrations ($n \geq 12$, $^*p \leq 0.0001$).

(J) The cardiac organoids under doxylamine succinate exposure showed no drug effects on the 3D organoid morphology at all the tested concentrations.

(K) Thalidomide exposure induced significant structural impairment on 3D organoid formation, showed as lower height ($n \geq 9$, $^*p \leq 0.0001$) and FWHM ($n \geq 14$, $^*p \leq 0.0001$) at high concentrations. Representative confocal projections of cardiac organoids at (K) untreated control and (M) 100 μM thalidomide exposure showed severe abnormal organoid formation for quantitative morphological scoring.

(N) Cardiac looping scored as a cardiac developmental toxicity evaluation in the zebrafish whole-embryo culture assay (zWEC) showed no significant drug effect from doxylamine succinate exposure, and a very mild toxicity level from high dosage exposure of thalidomide. A sample size of $n > 40$ embryos were analyzed for these treatment groups. In all panels, boxplots show the minimum, maximum, median, and 25th and 75th percentiles, and statistical ANOVA with Dunnett's multiple comparison test against controls. All data, including organoids and embryos, were pooled from three independent experiments.

Turnbull et al., 2018). These adult-mimicking model systems are designed to enhance the maturity of hiPSC-CMs for the purpose of drug screening and disease modeling, but not designed for studying dynamic cellular self-organization occurring along with the cardiac differentiation process. In contrast, stem cell-derived organoids are designed to resemble the early developing organs through self-organization of differentiating cells into spatial-distinct tissue-specific structures. However, cardiac organoids are still largely generated by aggregating pre-differentiated hiPSC-CMs with other stromal cells (Richards et al., 2017), instead of originating from directed stem cell differentiation. Our technique to generate cardiac organoids started with 2D micropatterned hiPSC colonies, allowing for cell self-organization into 3D tissue structures during the differentiation process under geometric confinement. Our new approach opens the possibility to create cardiac organoids that could resemble the similarity to a certain extent of biological process of tissue self-assembly and morphogenesis during early heart formation.

Commonly reported birth defects are heart related, and the potential for generating cardiac defects is a primary concern in determining drug developmental toxicity (Pamies et al., 2011). The cardiac organoid model allowed us to evaluate human-specific drug-induced developmental toxicity based on its disruption of forming correct 3D organoid structures and developing normal cardiac contractile functions. By exposing the cardiac organoids to a range of drugs with different risk, we found an overall increase of teratogenic severity on cardiac organoid formation, corresponding to an increase of test concentrations, and an increase of risk category from A to X. Especially, category D drugs (phenytoin, lithium, doxycycline, and tretinoin) showed diverse effects on developmental toxicity. Surprisingly, exposure of lithium only showed mild developmental toxicity of slight reduction in cardiac differentiation and organoid formation, although there has been a long debate of this drugs' developmental toxicity, especially resulting in congenital heart defects (Hoberman et al., 1990; Shaikh Qureshi et al., 2014).

Our drug response results of thalidomide were generally consistent with published works of embryotoxicity using both whole embryo and *in vitro* stem cell models. Previous work showed reduced cardiac differentiation efficiency in a hiPSC embryotoxicity test due to thalidomide treatment (Aikawa et al., 2014). A recent study demonstrated that thalidomide inhibited early mesoderm differentiation in chick embryos (Belair et al., 2020), which is the transitional stage during cardiac differentiation. From an embryoid body (EB)-based cardiac differentiation assay, thalidomide treatment showed decreased EB volume, similar to the decreased organoid height and FWHM from our cardiac organoids. Retinoids actually act as morphogens in embryogenesis, guiding gastrulation and body axis formation (Piersma et al., 2017). Overdose of retinoids has been linked to cardiovascular and skeletal developmental malformations (Collins and Mao, 1999). From iPSC models, retinoids impair metabolic responses involved in cell proliferation and differentiation (Palmer et al., 2017). In our study, retinoids impaired the cardiac differentiation but promoted the formation of giant tissues. It is possible that progenitor cells in our retinoid-treated organoids retained a high proliferative capacity to give rise large tissue growth, but inhibited the terminal differentiation of cardiomyocytes (Drowley et al., 2020). Another possibility is that the cells were directed to endoderm lineages, as exposure to these compounds was shown to severely disrupt mesoderm formation (Liu et al., 2018).

Embryotoxicity assays based on WEC have been invaluable in drug toxicology for decades, because they can study drug effects on whole systematic biological processes (Augustine-rauch et al., 2010). Generally, WEC assays focus on drug toxicity on structural and morphological features, such as limb and appendage malformations, but suffer from species differences that can lead to inaccurate predictions in humans (He et al., 2014). In contrast, stem cell-based assays, including mEST and newly developed *in vitro* platforms using human pluripotent stem cells, offer a cheaper and less-invasive methods to measure drug toxicity on mammalian and human cell differentiation (Seiler and Spielmann, 2011). However, they cannot characterize tissue morphogenesis and organ formation. In a comparison of triazole exposure to rat WEC, zebrafish WEC, and mEST, the zebrafish tests showed the best correlation, followed by mEST tests, regarding their toxicity levels relative to *in vivo* studies conducted in industry (de Jong et al., 2011). Rat WEC had the lowest correlation scores, which was likely caused by differences in drug exposure times calculated for each system, illustrating the challenges in embryotoxicity model comparisons. Other studies on embryotoxicity indicated a comparable result between WEC and mEST models, but poor correlation with *in vivo* reports (Dimopoulou et al., 2018; Inoue et al., 2016; Strikwold et al., 2012). Furthermore, these works suggest that a combination of different testing systems can provide better predictivity of embryotoxic potential. One study integrated mEST and zebrafish WEC to understand biological mechanisms of triclosan on early development (Chen et al., 2015), and found that triclosan causes developmental defects via disruption of pluripotent markers. In relation to the apparent heterogeneity of the cardiac organoids, we envision that the cardiac organoids can serve as complementary tests to current well-established assays to assess teratogenicity in both cell differentiation and tissue morphogenesis, which can provide a comprehensive risk-assessment toolkit to better predict drug toxicity on fetal health.

Recently, fully 3D heart organoids have been reported that form from Matrigel-embedded hPSC aggregates and develop into early heart and foregut endoderm tissues (Drakhlis et al., 2021). Although our method to micropattern hiPSCs and generate organoids is versatile and reproducible for various applications, one primary limitation is that the organoids are artificially attached to the substrate, instead of embodying a fully 3D culture system. Stimuli-responsive biomaterials can be explored in future to facilitate the on-demand detachment of organoids from the surface with proper triggering (e.g., temperature changes). Furthermore, the maturity of cardiac organoids has not been assessed, although we think the cardiomyocytes within our organoids are less mature compared with other engineered tissue model systems that applied different external stimulations to promote the maturation (Kolanowski et al., 2020; Nunes et al., 2013; Ronaldson-Bouchard et al., 2018). In addition, the presence of stromal cells in cardiac microtissues has been shown to promote maturity as well (Hookway et al., 2019). Currently, our model is purposed to studying early developmental events and drug effects on embryonic cardiogenesis, instead of mimicking adult-like physiology and drug responses. Future work to expand this study, such as lineage tracking, fate mapping, and single-cell genomic sequencing of organoids at different developmental stages, will reveal parallelism between human cardiac development and cardiac organoid formation through comprehensive molecular evidence. In the perspective of embryotoxicity assay development, our cardiac-based model system presents a major limitation in that it only focuses on cardiac differentiation as key assessment variables but cannot evaluate the developmental toxicity to a wide range of organ types (Seiler and Spielmann, 2011). Developmental toxicology can encompass a wide range of organ targets, depending on the molecular target of the specific drug, but may not particularly result in cardiac defects (Xu et al., 2020). Finally, many drug compounds are safe in their native chemical makeups, but undergo metabolism to produce toxic metabolites, which could lead to misclassifications of drug safety unless the screening can be achieved in a multi-organ system.

EXPERIMENTAL PROCEDURES

Cardiac organoid generation

Surface micropatterning on tissue culture polystyrene was carried out using the selective etching approach described previously (Hoang et al., 2018) (see supplemental information for detailed procedures). hiPSCs were cultured using standard PSC culture methods and seeded onto microfabricated wells at a density of approximately 0.63×10^5 cells/cm^2. Cardiac differentiation was initiated approximately 3 days after seeding (day 0) when the micropatterns reached confluency, and performed via small-molecule modulation of the Wnt/β-catenin pathway (Lian et al., 2012) with GSK3 inhibitor CHIR99021 (day 0) and WNT pathway inhibitor IWP4 (day 2).

Drug treatment

Drug stocks were prepared in water or DMSO, depending on solubility, and diluted to working concentrations in culture medium. Once initiated, the drugs were supplied continuously throughout the differentiation into cardiac organoids to mimic the continuous drug exposure during fetal development. Samples were terminated on day 20 for motion tracking analysis and for fluorescence/confocal imaging.

See supplemental information for detailed procedures, additional methods, and vendor information.

Data and code availability

Data requests and correspondence should be addressed to Z.M.

SUPPLEMENTAL INFORMATION

Supplemental information can be found online at https://doi.org/10.1016/j.stemcr.2021.03.013.

AUTHOR CONTRIBUTIONS

Z.M. and P.H. conceived the study and designed the experiments. P.H., S.S., and A.M.A. performed surface patterning and organoid generation-related experiments. S.S. acquired the data of GCaMP6f organoids and performed the calcium flux analysis. A.K. performed data mining on contractile function data from cardiac organoids. T.S.W. performed flow cytometry analysis. A.G.E.-C., A.R.G., W.L., and M.I.K. generated and provided the Yale WT hiPSC line for cell line comparison. P.H. performed all organoid-based drug toxicity studies. P.H. and J.D.A. performed zebrafish whole-embryo experiments. P.H. and S.M.L. collected and analyzed bulk motion tracking and image analysis datasets. P.H. and Z.M. wrote the manuscript with discussion and improvements from all authors. Z.M. supervised the project development and funded the study.

ACKNOWLEDGMENTS

We would like to thank the members of the Amack lab for their guidance with whole embryo experiments. This work was supported by the NIH NICHD (R01HD101130), NSF (CBET-1804875 and CBET-1943798), and SU Collaboration for Unprecedented Success and Excellence (CUSE) Grant. Z.M. acknowledges the support from Lush Prize Young Researchers at Americas. P.H. acknowledges support from the National Science Foundation Integrative Graduate Education and Research Traineeship (NSF IGERT) DMR-DGE-1068780 and the American Heart Association Predoctoral Fellowship (AHA 19PRE34380591).

ETHICS STATEMENT

All experiments using live zebrafish embryos were approved and performed in accordance with IACUC guidelines and regulations as directed by SUNY Upstate Medical University.

Received: August 12, 2020
Revised: March 13, 2021
Accepted: March 15, 2021
Published: May 11, 2021

REFERENCES

Ahler, E., Sullivan, W.J., Cass, A., Braas, D., York, A.G., Bensinger, S.J., Graeber, T.G., and Christofk, H.R. (2013). Doxycycline alters metabolism and proliferation of human cell lines. PLoS One *8*, e64561.

Aikawa, N., Kunisato, A., Nagao, K., Kusaka, H., Takaba, K., and Ohgami, K. (2014). Detection of thalidomide embryotoxicity by in vitro embryotoxicity testing based on human iPS cells. J. Pharmacol. Sci. *124*, 201–207.

Augustine-rauch, K., Zhang, C.X., and Panzica-kelly, J.M. (2010). In vitro developmental toxicology assays: a review of the state of the science of rodent and zebrafish whole embryo culture and embryonic stem cell assays. Birth Defects Res. C Embryo Today *98*, 87–98.

Belair, D.G., Lu, G., Waller, L.E., Gustin, J.A., Collins, N.D., and Kolaja, K.L. (2020). Thalidomide inhibits human iPSC mesendoderm differentiation by modulating CRBN-dependent degradation of SALL4. Sci. Rep. *10*, 2864.

Brassard, J.A., and Lutolf, M.P. (2019). Engineering stem cell self-organization to build better organoids. Cell Stem Cell *24*, 860–876.

Buss, W.C., Morgan, R., Guttmann, J., Barela, T., and Stalter, K. (1978). Rifampicin inhibition of protein synthesis in mammalian cells. Science *200*, 432 LP–434.

Chen, T.-W., Wardill, T.J., Sun, Y., Pulver, S.R., Renninger, S.L., Baohan, A., Schreiter, E.R., Kerr, R.A., Orger, M.B., Jayaraman, V., et al. (2013). Ultrasensitive fluorescent proteins for imaging neuronal activity. Nature *499*, 295–300.

Chen, X., Xu, B., Han, X., Mao, Z., Chen, M., Du, G., Talbot, P., Wang, X., and Xia, Y. (2015). The effects of triclosan on pluripotency factors and development of mouse embryonic stem cells and zebrafish. Arch. Toxicol. *89*, 635–646.

Collins, M.D., and Mao, G.E. (1999). Teratology of retinoids. Annu. Rev. Pharmacol. Toxicol. *39*, 399–430.

Czerniecki, S.M., Cruz, N.M., Harder, J.L., Menon, R., Annis, J., Otto, E.A., Gulieva, R.E., Islas, L.V., Kim, Y.K., Tran, L.M., et al. (2018). High-throughput screening enhances kidney organoid differentiation from human pluripotent stem cells and enables automated multidimensional phenotyping. Cell Stem Cell *22*, 929–940.e4.

Dimopoulou, M., Verhoef, A., Gomes, C.A., van Dongen, C.W., Rietjens, I.M.C.M., Piersma, A.H., and van Ravenzwaay, B. (2018). A comparison of the embryonic stem cell test and whole embryo culture assay combined with the BeWo placental passage model for predicting the embryotoxicity of azoles. Toxicol. Lett. *286*, 10–21.

Drakhlis, L., Biswanath, S., Farr, C.-M., Lupanow, V., Teske, J., Ritzenhoff, K., Franke, A., Manstein, F., Bolesani, E., Kempf, H., et al. (2021). Human heart-forming organoids recapitulate early heart and foregut development. Nat. Biotechnol. https://doi.org/10.1038/s41587-021-00815-9.

Drowley, L., McPheat, J., Nordqvist, A., Peel, S., Karlsson, U., Martinsson, S., Müllers, E., Dellsén, A., Knight, S., Barrett, I., et al. (2020). Discovery of retinoic acid receptor agonists as proliferators of cardiac progenitor cells through a phenotypic screening approach. Stem Cells Transl. Med. *9*, 47–60.

Fatehullah, A., Tan, S.H., and Barker, N. (2016). Organoids as an in vitro model of human development and disease. Nat. Cell Biol. *18*, 246–254.

He, J.H., Gao, J.M., Huang, C.J., and Li, C.Q. (2014). Zebrafish models for assessing developmental and reproductive toxicity. Neurotoxicol. Teratol. *42*, 35–42.

Hoang, P., Wang, J., Conklin, B.R., Healy, K.E., and Ma, Z. (2018). Generation of spatial-patterned early-developing cardiac organoids using human pluripotent stem cells. Nat. Protoc. *13*, 723–737.

Hoberman, A.M., Deprospo, J.R., Lochry, E.A., and Christian, M.S. (1990). Developmental toxicity study of orally administered lithium hypochlorite in rats. Int. J. Toxicol. *9*, 367–379.

Hookway, T.A., Matthys, O.B., Mendoza-Camacho, F.N., Rains, S., Sepulveda, J.E., Joy, D.A., and Mcdevitt, T.C. (2019). Phenotypic variation between stromal cells differentially impacts engineered cardiac tissue function. Tissue Eng. - Part A. *25*, 773–785.

Huang, C.J., Tu, C.T., Hsiao, C. Der, Hsieh, F.J., and Tsai, H.J. (2003). Germ-line transmission of a myocardium-specific GFP transgene reveals critical regulatory elements in the cardiac myosin light chain 2 promoter of zebrafish. Dev. Dyn. *228*, 30–40.

Huebsch, N., Loskill, P., Mandegar, M.A., Marks, N.C., Sheehan, A.S., Ma, Z., Mathur, A., Nguyen, T.N., Yoo, J.C., Judge, L.M., et al. (2015). Automated video-based analysis of contractility and calcium flux in human-induced pluripotent stem cell-derived cardiomyocytes cultured over different spatial scales. Tissue Eng. Part C Methods *21*, 467–479.

Huebsch, N., Loskill, P., Deveshwar, N., Spencer, C.I., Judge, L.M., Mandegar, M.A., Fox, C.B., Mohamed, T.M.A., Ma, Z., Mathur, A., et al. (2016). Miniaturized iPS-cell-derived cardiac muscles for physiologically relevant drug response analyses. Sci. Rep. *6*, 24726.

Hwang, N.S., Varghese, S., and Elisseeff, J. (2008). Controlled differentiation of stem cells. Adv. Drug Deliv. Rev. *60*, 199–214.

Inoue, A., Nishimura, Y., Matsumoto, N., Umemoto, N., Shimada, Y., Maruyama, T., Kayasuga, K., Morihara, M., Katagi, J., Shiroya, T., et al. (2016). Comparative study of the zebrafish embryonic toxicity test and mouse embryonic stem cell test to screen developmental toxicity of human pharmaceutical drugs. Fundam. Toxicol. Sci. *3*, 79–87.

de Jong, E., Barenys, M., Hermsen, S.A.B., Verhoef, A., Ossendorp, B.C., Bessems, J.G.M., and Piersma, A.H. (2011). Comparison of the mouse embryonic stem cell test, the rat whole embryo culture and the zebrafish embryotoxicity test as alternative methods for developmental toxicity testing of six 1,2,4-triazoles. Toxicol. Appl. Pharmacol. *253*, 103–111.

Kolanowski, T.J., Busek, M., Schubert, M., Dmitrieva, A., Binnewerg, B., Pöche, J., Fisher, K., Schmieder, F., Grünzner, S., Hansen, S., et al. (2020). Enhanced structural maturation of human induced pluripotent stem cell-derived cardiomyocytes under a controlled

microenvironment in a microfluidic system. Acta Biomater. *102*, 273–286.

Kumar, K.K., Aboud, A.A., and Bowman, A.B. (2012). The potential of induced pluripotent stem cells as a translational model for neurotoxicological risk. Neurotoxicology *33*, 518–529.

Lancaster, M.A., Corsini, N.S., Wolfinger, S., Gustafson, E.H., Phillips, A.W., Burkard, T.R., Otani, T., Livesey, F.J., and Knoblich, J.A. (2017). Guided self-organization and cortical plate formation in human brain organoids. Nat. Biotechnol. *35*, 659–666.

Lantz-McPeak, S., Guo, X., Cuevas, E., Dumas, M., Newport, G.D., Ali, S.F., Paule, M.G., and Kanungo, J. (2015). Developmental toxicity assay using high content screening of zebrafish embryos. J. Appl. Toxicol. *35*, 261–272.

Lee, L.M.Y., Leung, C.-Y., Tang, W.W.C., Choi, H.-L., Leung, Y.-C., McCaffery, P.J., Wang, C.-C., Woolf, A.S., and Shum, A.S.W. (2012). A paradoxical teratogenic mechanism for retinoic acid. Proc. Natl. Acad. Sci. *109*, 13668 LP–13673.

Li, P.-Y., Chang, Y.-C., Tzang, B.-S., Chen, C.-C., and Liu, Y.-C. (2007). Antibiotic amoxicillin induces DNA lesions in mammalian cells possibly via the reactive oxygen species. Mutat. Res. *629*, 133–139.

Lian, X., Hsiao, C., Wilson, G., Zhu, K., Hazeltine, L.B., Azarin, S.M., Raval, K.K., Zhang, J., Kamp, T.J., and Palecek, S.P. (2012). Robust cardiomyocyte differentiation from human pluripotent stem cells via temporal modulation of canonical Wnt signaling. Proc. Natl. Acad. Sci. U S A *109*, E1848–E1857.

Liu, Q., Van Bortle, K., Zhang, Y., Zhao, M.T., Zhang, J.Z., Geller, B.S., Gruber, J.J., Jiang, C., Wu, J.C., and Snyder, M.P. (2018). Disruption of mesoderm formation during cardiac differentiation due to developmental exposure to 13-cis-retinoic acid. Sci. Rep. *8*, 1–11.

Ma, Z., Wang, J., Loskill, P., Huebsch, N., Koo, S., Svedlund, F.L., Marks, N.C., Hua, E.W., Grigoropoulos, C.P., Conklin, B.R., et al. (2015). Self-organizing human cardiac microchambers mediated by geometric confinement. Nat. Commun. *6*, 7413.

Mandegar, M.A., Huebsch, N., Frolov, E.B., Shin, E., Truong, A., Olvera, M.P., Chan, A.H., Miyaoka, Y., Holmes, K., Spencer, C.I., et al. (2016). CRISPR interference efficiently induces specific and reversible gene silencing in human iPSCs. Cell Stem Cell *18*, 541–553.

Manfrin, A., Tabata, Y., Paquet, E.R., Vuaridel, A.R., Rivest, F.R., Naef, F., and Lutolf, M.P. (2019). Engineered signaling centers for the spatially controlled patterning of human pluripotent stem cells. Nat. Methods *16*, 640–648.

Morgani, S.M., Metzger, J.J., Nichols, J., Siggia, E.D., and Hadjantonakis, A.K. (2018). Micropattern differentiation of mouse pluripotent stem cells recapitulates embryo regionalized cell fate patterning. eLife *7*, 1–35.

Nunes, S.S., Miklas, J.W., Liu, J., Aschar-Sobbi, R., Xiao, Y., Zhang, B., Jiang, J., Massé, S., Gagliardi, M., Hsieh, A., et al. (2013). Biowire: a platform for maturation of human pluripotent stem cell-derived cardiomyocytes. Nat. Methods *10*, 781–787.

Ogle, B.M., Bursac, N., Domian, I., Huang, N.F., Menasché, P., Murry, C.E., Pruitt, B., Radisic, M., Wu, J.C., Wu, S.M., et al. (2016). Distilling complexity to advance cardiac tissue engineering. Sci. Transl. Med. *8*, 342ps13.

Palmer, J.A., Smith, A.M., Egnash, L.A., Colwell, M.R., Donley, E.L.R., Kirchner, F.R., and Burrier, R.E. (2017). A human induced pluripotent stem cell-based in vitro assay predicts developmental toxicity through a retinoic acid receptor-mediated pathway for a series of related retinoid analogues. Reprod. Toxicol. *73*, 350–361.

Pamies, D., Martínez, C.E., Sogorb, M.A., and Vilanova, E. (2011). Mechanism-Based Models in Reproductive and Developmental Toxicology (Elsevier Inc.).

Periasamy, M., and Janssen, P.M.L. (2008). Molecular basis of diastolic dysfunction. Heart Fail. Clin. *4*, 13–21.

Piersma, A.H., Hessel, E.V., and Staal, Y.C. (2017). Retinoic acid in developmental toxicology: teratogen, morphogen and biomarker. Reprod. Toxicol. *72*, 53–61.

Richards, D.J., Coyle, R.C., Tan, Y., Jia, J., Wong, K., Toomer, K., Menick, D.R., and Mei, Y. (2017). Inspiration from heart development: biomimetic development of functional human cardiac organoids. Biomaterials *142*, 112–123.

Rivron, N.C., Frias-Aldeguer, J., Vrij, E.J., Boisset, J.C., Korving, J., Vivié, J., Truckenmüller, R.K., Van Oudenaarden, A., Van Blitterswijk, C.A., and Geijsen, N. (2018). Blastocyst-like structures generated solely from stem cells. Nature *557*, 106–111.

Rodrigues, I.C.P., Kaasi, A., Maciel Filho, R., Jardini, A.L., and Gabriel, L.P. (2018). Cardiac tissue engineering: current state-of-the-art materials, cells and tissue formation. Einstein (Sao Paulo). *16*, eRB4538.

Ronaldson-Bouchard, K., Ma, S.P., Yeager, K., Chen, T., Song, L.J., Sirabella, D., Morikawa, K., Teles, D., Yazawa, M., and Vunjak-Novakovic, G. (2018). Advanced maturation of human cardiac tissue grown from pluripotent stem cells. Nature *556*, 239–243.

Sarmah, S., and Marrs, J.A. (2016). Zebrafish as a vertebrate model system to evaluate effects of environmental toxicants on cardiac development and function. Int. J. Mol. Sci. *17*, 2123.

Seiler, A.E.M., and Spielmann, H. (2011). The validated embryonic stem cell test to predict embryotoxicity in vitro. Nat. Protoc. *6*, 961–978.

Shaikh Qureshi, W.M., Latif, M.L., Parker, T.L., and Pratten, M.K. (2014). Lithium carbonate teratogenic effects in chick cardiomyocyte micromass system and mouse embryonic stem cell derived cardiomyocyte—possible protective role of myo-inositol. Reprod. Toxicol. *46*, 106–114.

Shao, Y., Sang, J., and Fu, J. (2015). On human pluripotent stem cell control: the rise of 3D bioengineering and mechanobiology. Biomaterials *52*, 26–43.

Strikwold, M., Woutersen, R.A., Spenkelink, B., Punt, A., and Rietjens, I.M.C.M. (2012). Relative embryotoxic potency of p-substituted phenols in the embryonic stem cell test (EST) and comparison to their toxic potency in vivo and in the whole embryo culture (WEC) assay. Toxicol. Lett. *213*, 235–242.

Tandon, S., and Jyoti, S. (2012). Embryonic stem cells: an alternative approach to developmental toxicity testing. J. Pharm. Bioallied Sci. *4*, 96–100.

Turnbull, I.C., Mayourian, J., Murphy, J.F., Stillitano, F., Ceholski, D.K., and Costa, K.D. (2018). Cardiac tissue engineering models of inherited and acquired cardiomyopathies. Methods Mol. Biol. *1816*, 145–159.

Warmflash, A., Sorre, B., Etoc, F., Siggia, E.D., and Brivanlou, A.H. (2014). A method to recapitulate early embryonic spatial patterning in human embryonic stem cells. Nat. Methods *11*, 847–854.

Weber, T., Auer, J., O'Rourke, M.F., Punzengruber, C., Kvas, E., and Eber, B. (2006). Prolonged mechanical systole and increased arterial wave reflections in diastolic dysfunction. Heart *92*, 1616–1622.

Xu, T., Wu, L., Xia, M., Simeonov, A., and Huang, R. (2020). Systematic identification of molecular targets and pathways related to human organ level toxicity. Chem. Res. Toxicol.

Zheng, Y., Xue, X., Shao, Y., Wang, S., Esfahani, S.N., Li, Z., Muncie, J.M., Lakins, J.N., Weaver, V.M., Gumucio, D.L., et al. (2019). Controlled modelling of human epiblast and amnion development using stem cells. Nature *573*, 421–425.

Stem Cell Reports, Volume *16*

Supplemental Information

Engineering spatial-organized cardiac organoids for developmental toxicity testing

Plansky Hoang, Andrew Kowalczewski, Shiyang Sun, Tackla S. Winston, Adriana M. Archilla, Stephanie M. Lemus, A. Gulhan Ercan-Sencicek, Abha R. Gupta, Wenzhong Liu, Maria I. Kontaridis, Jeffrey D. Amack, and Zhen Ma

Supplemental Figures

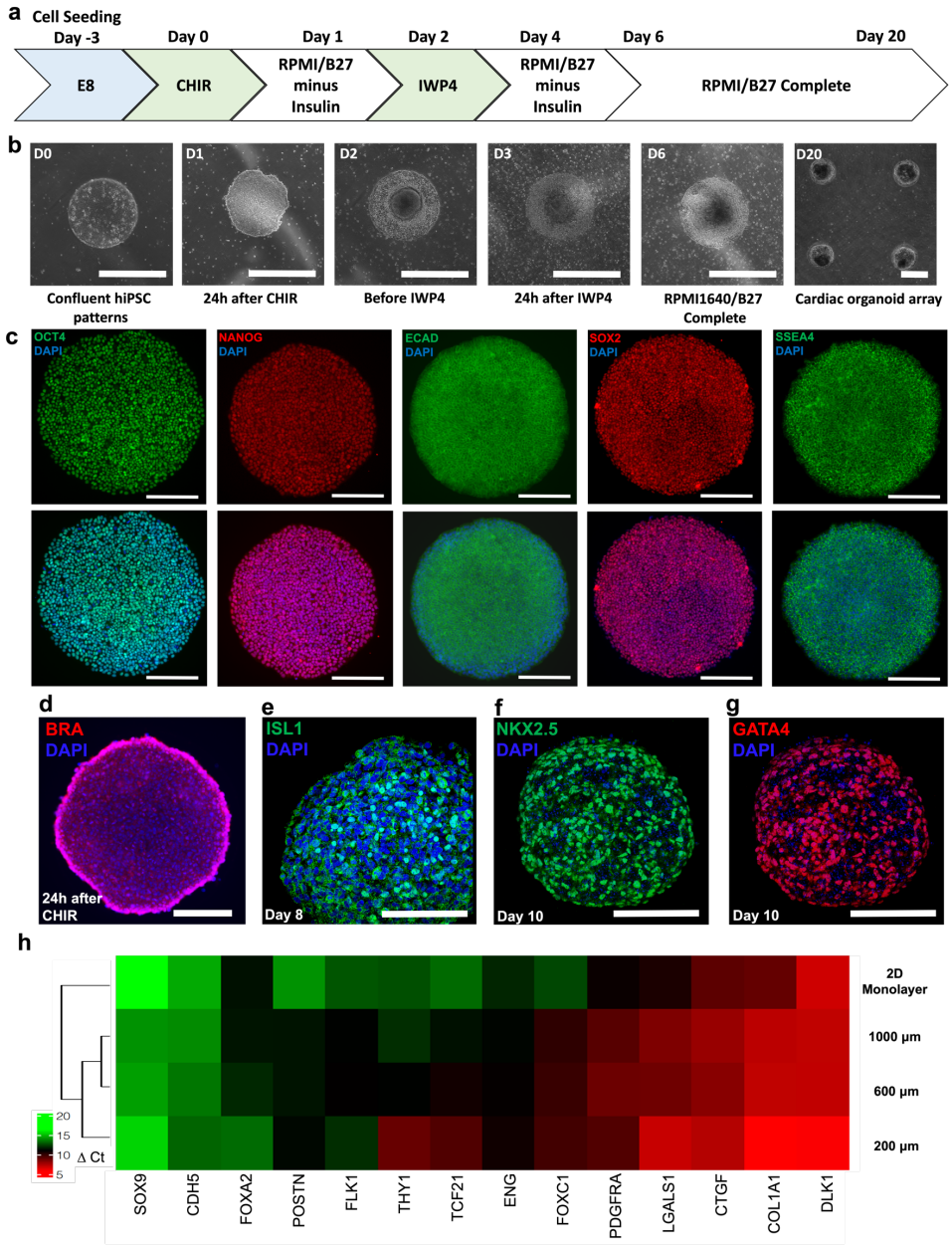

Supplemental Figure 1. *(a) Cardiac differentiation timeline to generate cardiac organoids. (b) Patterned cell morphology changes from 2D monolayer of cells (D0) into 3D tissue (D6 onward) throughout differentiation; scale bars 600 µm. (c) Patterned hiPSCs retain expression of pluripotent markers when confluent (From left to right: OCT4, NANOG, ECAD, SOX2, SSEA4. (d) 24h after CHIR treatment, patterned hiPSCs express mesodermal marker brachyury. (e) On Day 8 of differentiation, cardiac organoids express ISL1, followed by (f) NKX2.5 and (g) GATA4 on Day 10, indicative of early cardiac progenitor cells. (h) Stromal gene expression illustrates higher upregulation of stromal markers in organoids relative to 2D monolayer differentiation and higher upregulation of stromal cell makers in 200-µm organoids relative to 600-µm and 1000-µm organoids. ΔCt values were calculated relative to the average Ct of GAPDH and 18S housekeeping controls. Scale bars 200 µm.*

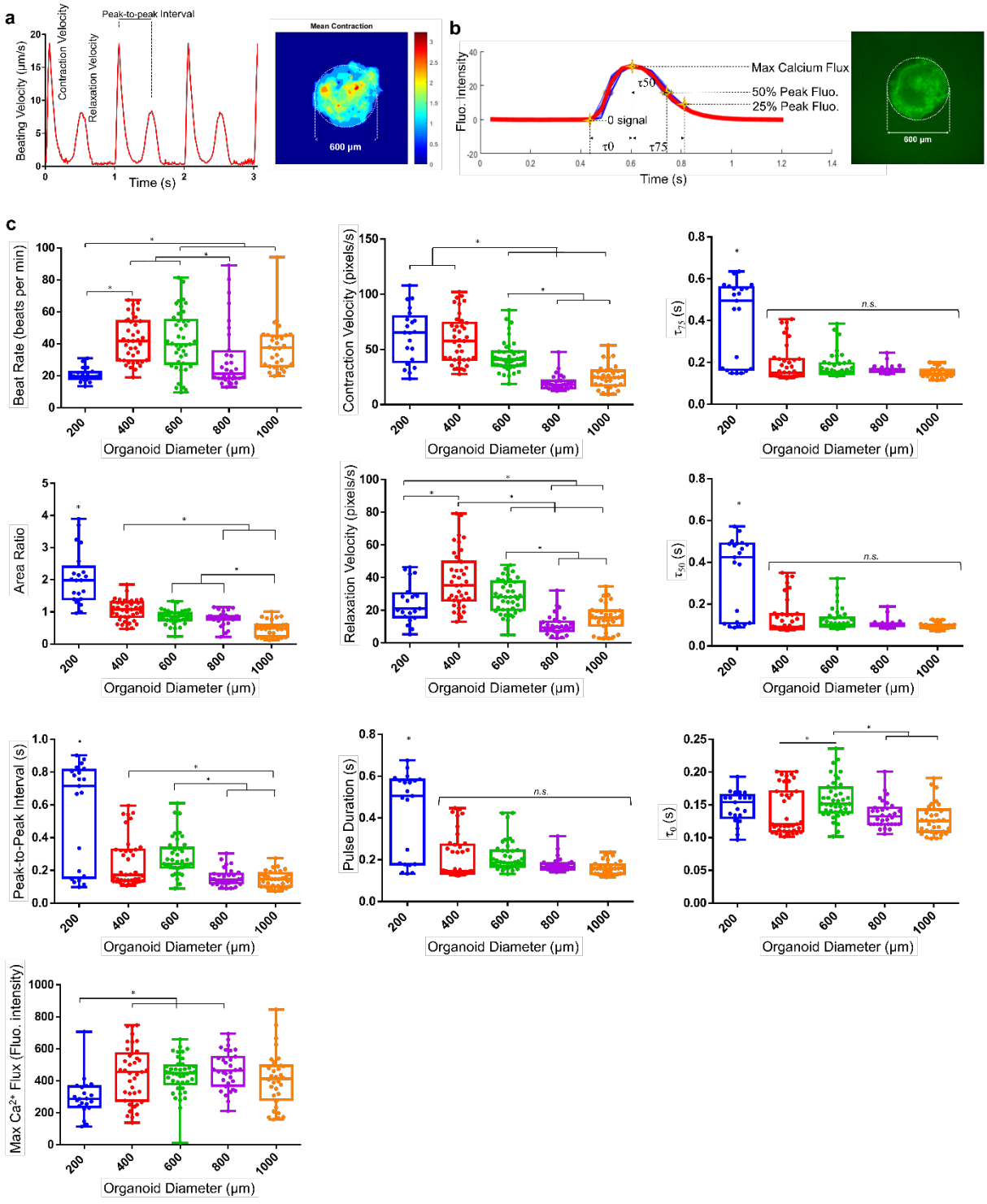

Supplemental Figure 2. *Contraction function analysis of cardiac organoids generated from GCaMP6f hiPSCs. Videos of beating organoids were characterized with using motion tracking analysis to generate (a) motion waveform where each double-peak represents a contraction-relaxation cycle. The Peak-to-peak interval describes the time between the contraction and relaxation peaks. (b) Transient calcium flux signals were acquired from capturing videos of GCaMP6f cardiac organoids and plotting z-axis profiles using ImageJ. Fluorescence bleaching (descending blue*

signal) was corrected (red signal) using in-house MATLAB scripts. Time decay parameters τ_0, τ_{50}, and τ_{75} were acquired by measuring time intervals from the signal initiation to the maximum calcium flux (τ_0), for the maximum flux to decay to 50% (τ_{50}), and for the maximum flux to decay to 25% (τ_{75}). All figures represent schematic illustrations of characterization parameters. (c) Raw data metrics used for data mining and tSNE clustering of organoid contraction functions. Individual points for each variable are shown to illustrate sample distribution. Comparable trends are seen where small patterns significantly prolong the beat duration, based on metrics τ_{75}, τ_{50}, peak-to-peak interval and pulse duration. This can be correlated to the area ratio, which is also significantly greater in small 200 μm organoids. Moreover, most variables illustrated some degree of pattern size dependency, with the most significant functional variations seen in 200 μm organoids. All statistics analyzed using ANOVA with Tukey multiple comparison tests. $p \leq 0.05$ is considered significant (*).

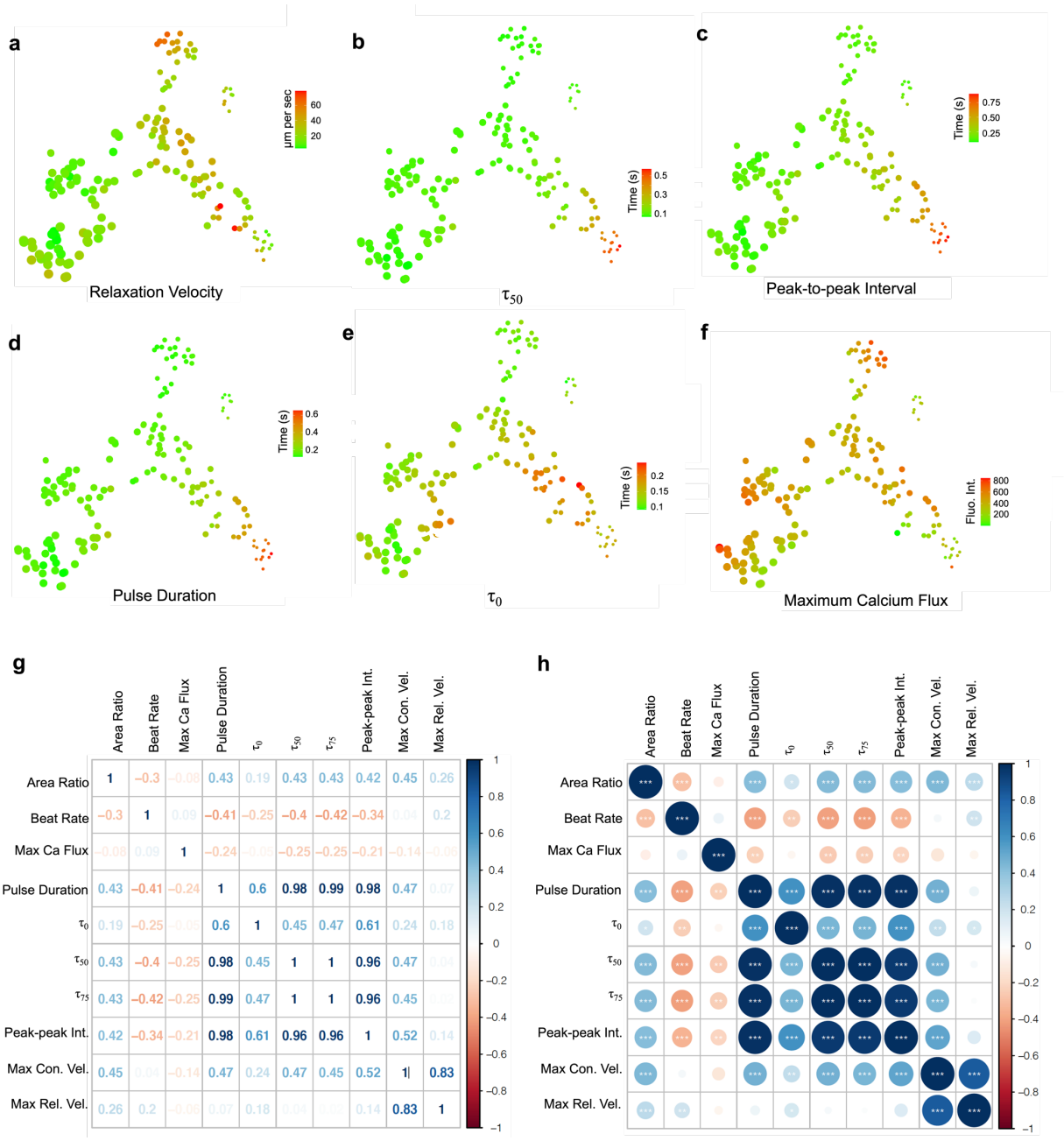

Supplemental Figure 3. *t-SNE gradient plots of contraction functions of cardiac organoids. Contraction function was plotted using co!or gradients to illustrate the influence of organoid size on (a) relaxation velocity, (b) τ_{50}, (c) peak-peak-interval, (d) pulse duration, (e) τ_0, and (f) maximum calcium flux. Small organoids primarily exhibited longer contraction duration cycles, as indicated by higher values in relaxation velocity, τ_{50}, peak-to-peak interval, and pulse duration. All organoids exhibited comparable patterns of maximum calcium flux, indicating that size did not impair the cardiac organoid ability to attain peak contraction. (g) Correlation coefficients showing individual variables correlation with other variable. A correlation coefficient closer to 1 is equivalent to positive correlation, where negative correlation is associated with values close to -1. (h) P-value representation of correlation coefficient significance. (*) denotes $p \leq 0.05$; (**) denotes $p \leq 0.01$; (***) denotes $p \leq 0.001$.*

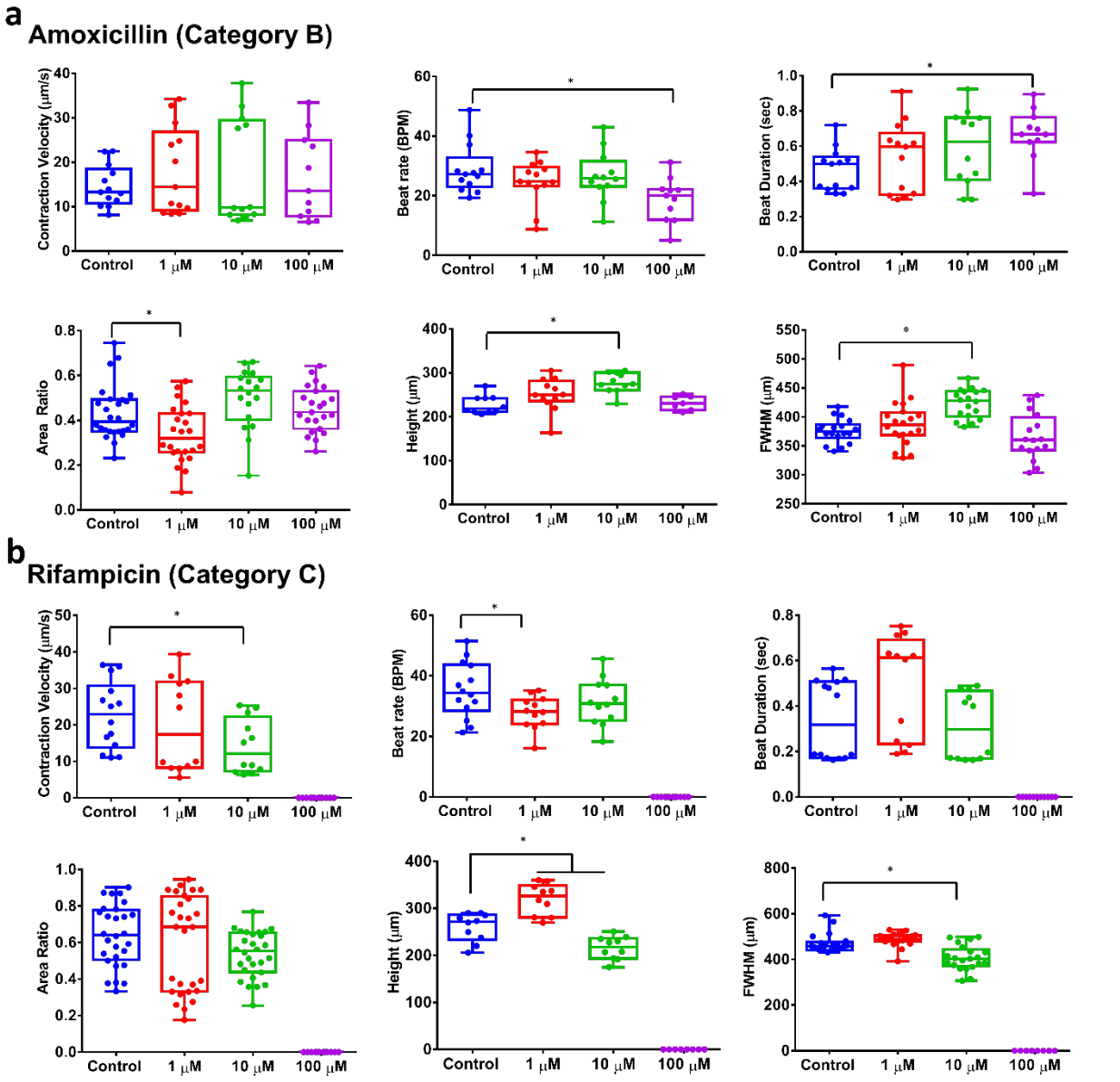

Supplemental Figure 4. *Developmental toxicity assay of cardiac organoids in response to treatment with Category B and C drugs. (a) Amoxicillin showed moderate toxicity with decreased beat rate (ANOVA, n ≥ 11, *p = 0.0215) and increased beat duration (ANOVA, n ≥ 11, *p = 0.0484) at high concentrations. Amoxicillin treatment at low concentrations, however, produced smaller cardiac tissues in area ratio (ANOVA, n ≥ 18, *p = 0.0003 between Controls and 1 μM), height (ANOVA, n ≥ 7, *p = 0.0006), and FWHM (ANOVA, n≥16, *p ≤ 0.0001). (b) Developmental toxicity assay of cardiac organoids in response to treatment with Category C drug, Rifampicin. In all assays, cardiac organoids failed to differentiate at 100 μM treatment, and toxicity was also observed in contraction velocity (ANOVA, n ≥ 12, *p <0.0001), beat rate (ANOVA, n ≥ 12, *p < 0.05), height (ANOVA, n ≥ 10, *p ≤ 0.05) and in FWHM (ANOVA, n ≥ 21, *p < 0.05).*

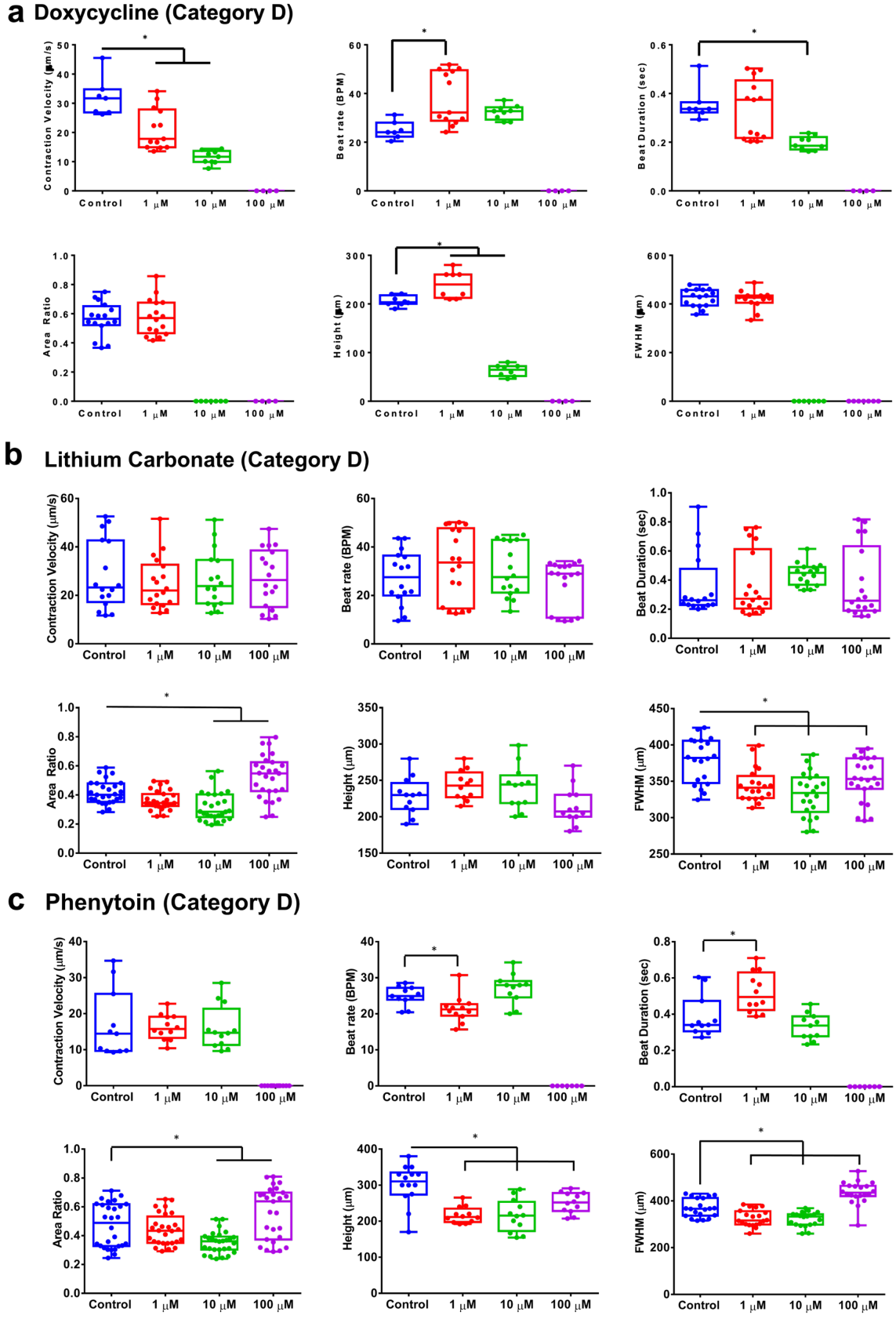
a Doxycycline (Category D)
Contraction Velocity (μm/s)
Beat rate (BPM)
Beat Duration (sec)
Area Ratio
Height (μm)
FWHM (μm)
b Lithium Carbonate (Category D)
Contraction Velocity (μm/s)
Beat rate (BPM)
Beat Duration (sec)
Area Ratio
Height (μm)
FWHM (μm)
c Phenytoin (Category D)
Contraction Velocity (μm/s)
Beat rate (BPM)
Beat Duration (sec)
Area Ratio
Height (μm)
FWHM (μm)
Control
1 μM
10 μM
100 μM
*

Supplemental Figure 5. *Developmental toxicity assay of cardiac organoids in response to treatment with Category D drugs. (a) With doxycycline treatment, cardiac organoids failed to differentiate at 100 μM treatment, and did not form robust cardiac tissues at 10 μM. Significant toxicity was observed in contraction velocity (ANOVA, $n \geq 7$, $^*p < 0.05$), beat rate (ANOVA, $n \geq 7$, $^*p < 0.05$), beat duration (ANOVA, $n \geq 7$, $^*p \leq 0.0001$), and height (ANOVA, $n = 8$, $^*p$ 0.05 relative to controls) and in FWHM (ANOVA, $n \geq 21$, $^*p < 0.05$). (b) With lithium carbonate treatment, no significant toxicity effects were seen in any contraction function. However, moderate toxicity was seen in higher concentrations for the area ratio (ANOVA, $n \geq 26$, $^*p \leq 0.0001$) and in FWHM (ANOVA, $n \geq 20$, $^*p \leq 0.0001$) relative to the controls. (c) Phenytoin showed no contractile functions at 100 μM concentration, with moderate effects at 1 μM on beat rate (ANOVA, $n \geq 11$, $^*p < 0.0001$) and beat duration (ANOVA, $n \geq 11$, $^*p < 0.0001$). Organoids were also smaller in area ratio at 10 μM treatment (ANOVA, $n = 28$, $^*p < 0.0001$) and smaller at all concentrations in height (ANOVA, $n \geq 12$, $^*p \leq 0.0001$) and at low and moderate concentrations in FWHM (ANOVA, $n=20$, $^*p \leq 0.0001$) relative to controls.*

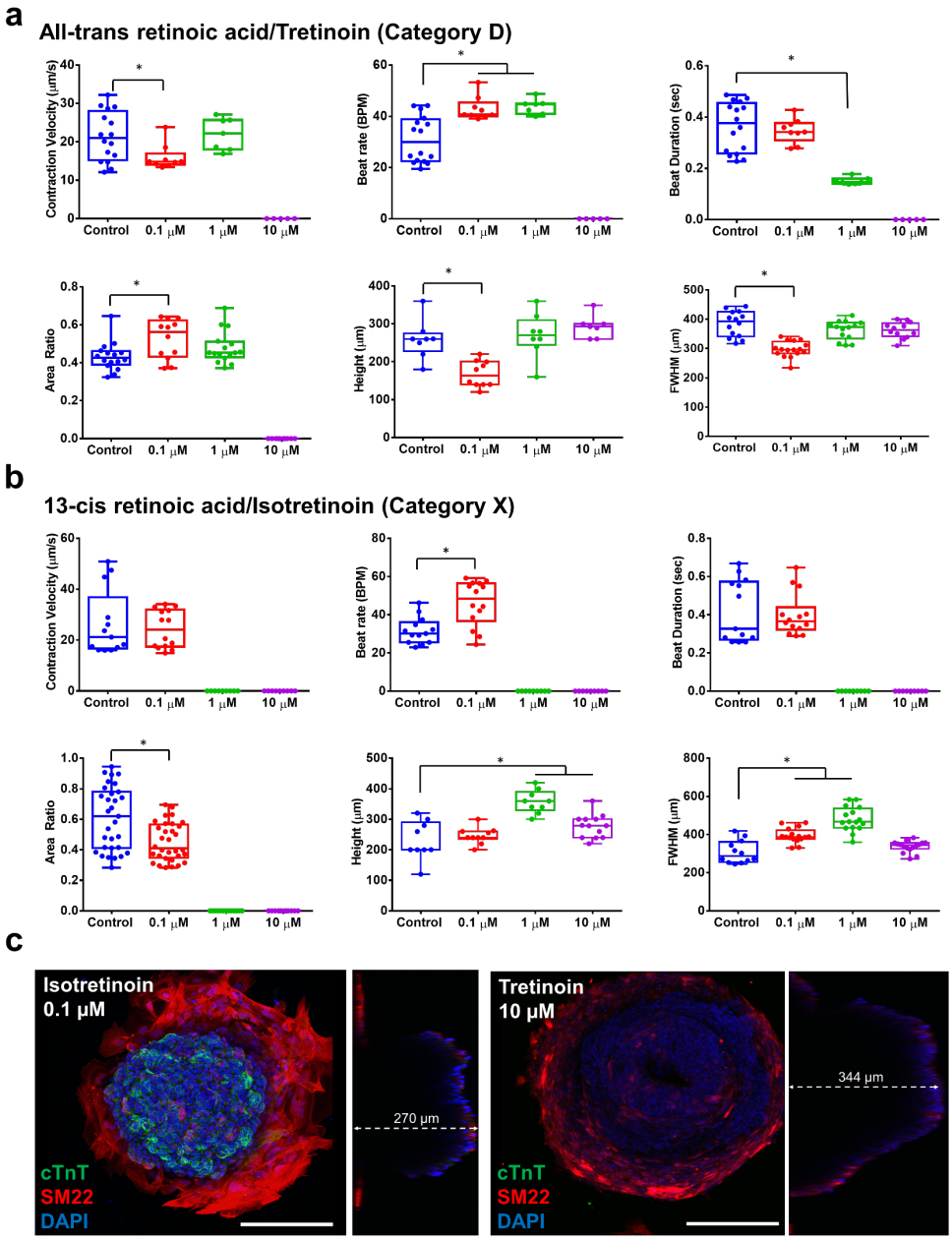

Supplemental Figure 6. *Developmental toxicity assay of cardiac organoids in response to treatment with retinoids Tretinoin (Category D) and Isotretinoin (Category X). (a) With tretinoin, cardiac tissue failed to differentiate at 10 μM concentrations with no contraction functions. Contraction velocity was lower at 0.1 μM (ANOVA, n ≥ 7, *p < 0.0001), whereas beat rate was faster at 0.1μM and 1 μM (ANOVA, n ≥ 7, *p < 0.0001). Beat duration was significantly lower at 1 μM (ANOVA, n ≥ 7, *p ≤ 0.0001) as well. Low concentration of 0.1 μM also showed toxic effects on area ratio (ANOVA, n ≥ 12, *p ≤ 0.0001), height (ANOVA, n ≥ 8, *p < 0.0001), and FWHM (ANOVA, n ≥ 12, *p ≤ 0.0001). (b) Cardiac tissue failed to develop at 1 μM and 10 μM concentrations with no contraction functions. Low concentration of 1 μM resulted in faster beat rate (ANOVA, n ≥ 13, *p ≤ 0.0001) and smaller area ratio (ANOVA, n ≥ 31, *p ≤ 0.0001). However, high concentrations produced organoids that were significantly taller in height (ANOVA, n ≥ 9, *p ≤ 0.0001) and larger in FWHM (ANOVA, n ≥ 12, *p ≤ 0.0001). (c) Representative images show cardiac tissue formation at low (0.1 μM) concentration, but a large mound with no cardiac tissue at high (10 μM) concentration of retinoid exposures. Scale bars 200 μm.*

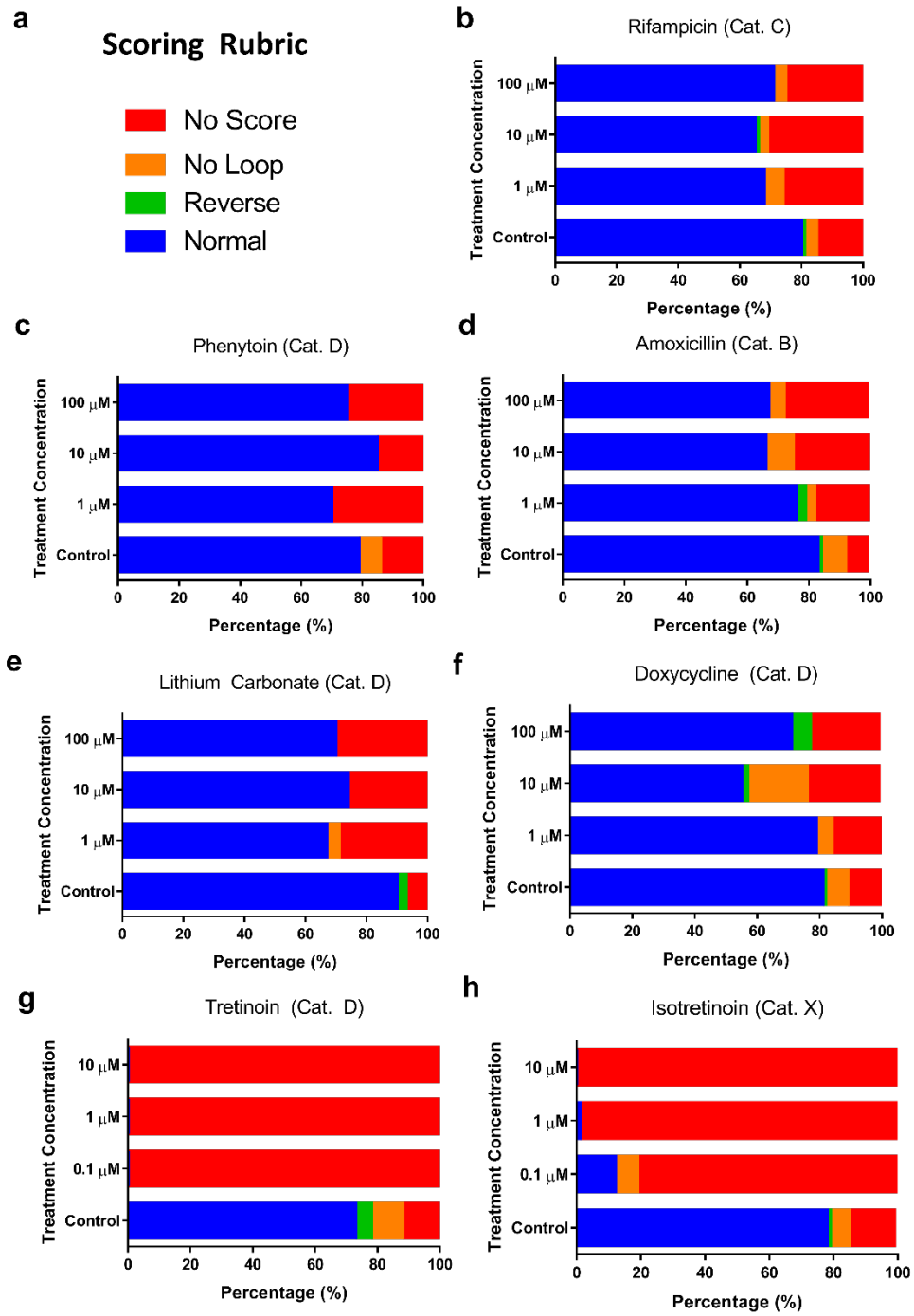

Supplemental Figure 7. *Zebrafish whole embryo culture (zWEC) assay of cardiac looping for seven drug compounds. (a) Morphological scoring was performed on heart structures of developing zebrafish embryos based on either normal (D-loop), reverse (L-loop), no loop, or no score where the heart did not express GFP and/or fall into the previous three categories. (b) Category C rifampicin and (c) Category D phenytoin produced mild developmental toxic effect. (d-f) Various drugs displayed moderate developmental toxicity amoxicillin (Category B), lithum carbonate (Category D), and doxycycline (Category D). Retinoids (g) Category D tretinoin and (h) Category X isotretnoin produced severe developmental toxic effects at all concentrations. (h) A sample size of n>19 embryos (pooled from 3 independent experiments) was used for all treatment groups.*

Supplemental Movies

Supplemental Movie 1. Three-dimensional confocal microscopy reconstructions of a cardiac organoids of 200 µm diameter (left), 600 µm diameter (middle), and 1000 µm diameter (right).

Supplemental Movie 2. Cross sectional reconstructions in z-direction of cardiac organoids of 200 µm diameter (left), 600 µm diameter (middle), and 1000 µm diameter (right).

Supplemental Movie 3. Cardiac organoids of 200 µm diameter (left), 600 µm diameter (middle), and 1000 µm diameter (right) exhibiting spontaneous contraction.

Supplemental Movie 4. Transient calcium flux of cardiac organoids of 200 µm diameter (left), 600 µm diameter (middle), and 1000 µm diameter (right).

Supplemental Tables

Supplemental Table 1. List of drug compounds with medicinal uses and previously designated pregnancy category.

Drug	Medicinal Use	Pregnancy Category	Concentrations Tested
Doxylamine Succinate	Antihistamine, sleeping aid	A	1 μM, 10 μM, 100 μM
Amoxicillin	Antibiotic (strep, middle ear infections etc.)	B	1 μM, 10 μM, 100 μM
Rifampicin	Antibiotic (TB, leprosy etc.)	C	1 μM, 10 μM, 100 μM
Lithium Carbonate	Bipolar antidepressant	D	1 μM, 10 μM, 100 μM
Phenytoin	Anticonvulsant	D	1 μM, 10 μM, 100 μM
Doxycycline	Antibiotic	D	1 μM, 10 μM, 100 μM
All-trans-RA (Tretinoin)	Acne treatment	D	0.1 μM, 1 μM, 10 μM
13-cis-RA (Isotretinoin)	Acne treatment	X	0.1 μM, 1 μM, 10 μM
Thalidomide	Myeloma, Inflammation	X	1 μM, 10 μM, 100 μM

Supplemental Table 2. List of primary and secondary antibodies used for immunofluorescent staining and imaging.

Primary antibodies (species)	Vendor	Catalog No.	Dilution
Cardiac troponin T (mouse)	Thermo Fisher Scientific	MS295P	1:200
Sarcomeric α-actinin (mouse)	Sigma-Aldrich	A7811	1:300
Myosin heavy chain (mouse)	Abcam	Ab97715	1:200
Cardiac troponin I (rabbit)	Abcam	Ab47003	1:200
Vimentin (mouse)	Thermo Fisher Scientific	MA5-11883	1:100
α-SM22 (rabbit)	Abcam	Ab14106	1:300
Calponin (rabbit)	Abcam	Ab46794	1:200
α-Smooth muscle actin (rabbit)	Abcam	Ab5694	1:100
OCT4 (rabbit)	Abcam	Ab18976	1:200
NANOG (mouse)	Thermo Fisher Scientific	MA1-017	1:100
SSEA4 (mouse)	Stem Cell Technologies	60062	1:200
SOX2 (rabbit)	Thermo Fisher Scientific	PA1-094	1:100
E-cadherin (mouse)	Abcam	Ab1416	1:200
Secondary Antibodies			
Alexa Fluor 488 goat anti-mouse	Thermo Fisher Scientific	A-11029	1:200
Alexa Fluor 546 goat anti-mouse	Thermo Fisher Scientific	A11003	1:200
Alexa Fluor 488 goat anti-rabbit	Thermo Fisher Scientific	A11008	1:200
Alexa Fluor 546 goat anti-rabbit	Thermo Fisher Scientific	A11010	1:200

Supplemental Table 3. TaqMan arrays used for cardiogenic and stromal gene expression analyses

Taqman Assay ID	Gene/Array Name	Taqman Assay ID	Gene/Array Name
Hs00153836_m1	ACVR1	Hs00276431_m1	NOX4
Hs00923299_m1	ACVR1B	Hs00383231_m1	NPPA
Hs00155658_m1	ACVR2A	Hs00173590_m1	NPPB
Hs00609603_m1	ACVR2B	Hs00176973_m1	PRKCA
Hs00181051_m1	APC	Hs00176998_m1	PRKCB
Hs00153179_m1	ATF2	Hs01090047_m1	PRKCD
Hs00394718_m1	AXIN1	Hs00178455_m1	PRKCE
Hs00205566_m1	BMP10	Hs00177010_m1	PRKCG
Hs00154192_m1	BMP2	Hs00702254_s1	PRKCI
Hs00370078_m1	BMP4	Hs00989970_m1	PRKCQ
Hs00233476_m1	BMP7	Hs00177051_m1	PRKCZ
Hs01034913_g1	BMPR1A	Hs01078066_m1	RB1
Hs00176144_m1	BMPR1B	Hs00195432_m1	SMAD1
Hs00176148_m1	BMPR2	Hs00183425_m1	SMAD2
Hs01026536_m1	CCNE1	Hs00929647_m1	SMAD4
Hs00372959_m1	CCNE2	Hs00195437_m1	SMAD5
Hs00154374_m1	CDC6	Hs00195441_m1	SMAD9
Hs00270923_s1	CEBPB	Hs00396596_m1	TBX20
Hs00193796_m1	CER1	Hs01052563_m1	TBX5
Hs00175141_m1	CHUK	Hs00413032_m1	TCF3
Hs00355045_m1	CTNNB1	Hs01009038_m1	TCF7L2
Hs00183740_m1	DKK1	Hs02339499_g1	TDGF1
Hs00737028_m1	DVL1	Hs00998133_m1	TGFB1
Hs00153451_m1	E2F1	Hs00234244_m1	TGFB2
Hs00231667_m1	E2F2	Hs01086000_m1	TGFB3
Hs00605457_m1	E2F3	Hs00610318_m1	TGFBR1
Hs00608098_m1	E2F4	Hs00234253_m1	TGFBR2
Hs00231092_m1	E2F5	Hs00182986_m1	WNT11
Hs00242501_m1	E2F6	Hs00263977_m1	WNT3A
Hs00266645_m1	FGF2	Hs00230534_m1	WNT8A
Hs00268943_s1	FZD1	Hs00610126_m1	WNT8B
Hs00273077_s1	FZD10	Hs00426835_g1	ACTA2
Hs00184043_m1	FZD3	Hs00901465_m1	CDH5
Hs00201853_m1	FZD4	Hs00959434_m1	CNN1
Hs00361869_g1	FZD5	Hs00164004_m1	COL1A1
Hs00171574_m1	FZD6	Hs00170014_m1	CTGF
Hs00275833_s1	FZD7	Hs00171584_m1	DLK1
Hs00259040_s1	FZD8	Hs00923996_m1	ENG
Hs00171403_m1	GATA4	Hs00911700_m1	FLK1
Hs01053355_m1	GNAI1	Hs00232764_m1	FOXA2
Hs01064686_m1	GNAI2	Hs00559473_s1	FOXC1
Hs00197803_m1	GNAI3	Hs00355202_m1	LGALS1
Hs00387073_m1	GNAQ	Hs01101425_m1	MYH6
Hs00255603_m1	GNAS	Hs04187281_m1	MYL4
Hs01564092_m1	GNB3	Hs00998018_m1	PDGFRA
Hs00275656_m1	GSK3B	Hs01065279_m1	PECAM1
Hs00231848_m1	HAND1	Hs01566750_m1	POSTN
Hs00232769_m1	HAND2	Hs00165814_m1	SOX9
Hs00167041_m1	HNF1A	Hs01038777_g1	TAGLN
Hs01001602_m1	HNF1B	Hs01385457_m1	TBX18
Hs00230853_m1	HNF4A	Hs00911929_m1	TBX2
Hs00212390_m1	LEF1	Hs00162646_m1	TCF21
Hs00745761_s1	LEFTY2	Hs00174816_m1	THY1
Hs00177373_m1	MAP3K7	Hs00165957_m1	TNNI3
Hs00176247_m1	MAPK14	Hs00943911_m1	TNNT2
Hs00231149_m1	MEF2C	Hs00958111_m1	VIM
Hs01110632_m1	MYH7	Hs01103751_m1	WT1
Hs00293096_m1	MYH7B	Hs99999905_m1	GAPDH (HK)
Hs00166405_m1	MYL2	Hs99999909_m1	HPRT1 (HK)
Hs00231763_m1	NKX2-5	Hs99999908_m1	GUSB (HK)
Hs00415443_m1	NODAL	Hs99999901_s1	18S (HK)

Experimental Procedures

Micropatterning of tissue culture surfaces

Surface micropatterning on tissue culture polystyrene was carried out using the selective etching approach described previously (Hoang et al., 2018). Patterned wafers were (SU8 master) fabricated using standard SU8 photolithography to fabricate molds with raised features of patterns. Poly(dimethyl siloxane) (PDMS) prepared at a 10:1 wt/wt ratio of elastomer base to curing agent was casted onto SU8 masters and clamped down using clear transparency sheets and glass slides. This process produced thin PDMS stencils with clear-through holes from the raised patterns on the SU8 master molds. Non-fouling poly(ethylene glycol) (PEG) solution was prepared by combining 150 mg PEG 1000 (Polysciences, cat. no. 16666), 1.8 mL PEGDA 400 (Polysciences, cat. no. 01871), 14.55 mL isopropyl alcohol, and 0.45 mL MilliQ water. The solution was grafted onto 6-well tissue culture plates and cured under UV light exposure (Dymax UV Illuminator; model no. 2000EC) for 45 seconds. Micropatterns were fabricated by selective oxygen plasma etching (Oxygen plasma treatment system, PlasmaEtch PE50XL) of the PEG using the PDMS stencils. Micropatterned tissue culture plates were sterilized by immersing in 70% ethanol for 1 hour and subsequent washing with sterile phosphate buffered saline (PBS).

Cell lines

Wild-type (WTC) hiPSC line was obtained from Dr. Conklin's laboratory at the Gladstone Institute of Cardiovascular Research. This hiPSC line was derived from a skin biopsy from a healthy adult Asian male donor in his early thirties. The original fibroblasts were reprogrammed using episomal methods with the factors of LIN28A, MYC (c-MYC), POU5F1 (OCT4) and SOX2. WTC GCaMPf6 hiPSC line was generated in Dr. Conklin's laboratory by targeting to the AAVS1 locus of WTC cells. A strong constitutive promoter (CAG) drives the expression of the GCaMP6f ORF. Yale-WT hiPSCs line was obtained from Dr. Abha Gupta's laboratory at the Yale University Department of Pediatrics and Child Study Center. Briefly hiPSCs were generated from the T-lymphocytes of a 25-year-old healthy South Asian male using the CytoTune-iPS Sendai Reprogramming kit as described previously (Liu et al., 2019).

Generation of cardiac organoids

Micropatterned surfaces were coated with diluted Geltrex hESC-qualified matrix (Life Technologies, cat. no. A1413302) at 37 ˚C for 1 hour prior to cell seeding. hiPSCs were cultured using standard PSC practices in Essential 8 (E8) medium (Life Technologies, cat. no. A1517001). At passaging confluency, cells were dissociated with Accutase (Life Technologies, cat. no. A1110501) and seeded at a density of $6.0x10^5$ cells per well of the micropatterned 6-well plate (~$0.63x10^5$ cells per cm^2) supplemented with 10 μM Y27632 (BioVision, cat. no. 1784-5). Cardiac differentiation was initiated approximately 3 days after seeding (Day 0) when the micropatterns reached confluency, and performed via small molecule modulation of the Wnt/β-catenin pathway (Lian et al., 2012) with GSK3 inhibitor CHIR99021 (Day 0) (Stemgent, cat. no. 04-0004) and WNT pathway inhibitor IWP4 (Day 2) (Stemgent, cat. no. 04-0036). Small molecules were diluted in in RPMI 1640 medium (Life Technologies, cat. no. 11875093) supplemented with B27-minus insulin (RPMI/B27 minus insulin) (Life technologies, cat. no. A1895601). Cardiac organoids began to contract around Day 9 of differentiation and were maintained in RPMI 1640 medium supplemented with complete B27 supplement (RPMI/B27 Complete) (Life Technologies cat. no. 17504044) until Day 20 for contractile and structural analysis.

Gene Expression Analysis

Gene expression was quantified using real-time qPCR analysis. On Day 20 of differentiation, cardiac organoids were sacrificed for RT-qPCR analysis. RNA was extracted using the RNeasy Mini Kit (Qiagen cat. no. 74104) and stored in -80 ˚C until needed. The RNA was then converted to cDNA using the Superscript IV First Strand Synthesis kit (Thermofisher cat. no. 18091050). Genes of interest includes cardiomyocyte-specific genes and stromal cell genes, plus TaqMan array of human factors for cardiogenesis (Thermofisher cat. no. 4414134). Individual genes are listed in the Supplemental Table 3. PCR plates were prepared and then run using the QuantStudio 3 Real-Time PCR System. All data was normalized to the respective housekeeping genes that were run in parallel with the rest of the gene assays. Value of ΔCt was

calculated by subtracting the average Ct of housekeeping genes from the Ct of the genes of interest. Lower ΔCt indicates gene upregulation, where high ΔCt indicates gene downregulation.

Flow Cytometry Analysis

Cardiac organoids were dissociated using 0.25% Trypsin for 10-15 minutes. Cells were collected, centrifuged and washed with PBS. Cells were fixed and permeabilized with a mixture of 4% (vol/vol) paraformaldehyde and 0.2% (vol/vol) TritonX solution for 15 minutes. Cells were incubated with primary antibody cardiac troponin T (Thermofisher cat. no. MA5-12960) in a 1:250 dilution for 1 hour in PBS, and then incubated with AlexaFluor 546 secondary fluorophore for an additional hour. The cell suspension was washed, centrifuged and filtered through 35 μm mesh cell strainer. Flow cytometry was performed on the BDAccuriC6 at Flow Cytometry Core at Syracuse University

Drug treatment

Concentrations were chosen after evaluation of blood plasma concentrations reported for each drug from the FDA drug information database (accessdata.FDA.gov). Concentrations were chosen to be at or approximated by blood plasma concentrations, while accounting for drug solubility in water or DMSO, while also supplying a large range in order to detect potential toxicity. Drugs were diluted in the appropriate culture media at three concentrations each increasing by a factor of 10 with respective controls. Control samples were supplemented with water or DMSO (≤ 0.1%), depending on the solvent used to prepare the concentrated stock. Once initiated, the drugs were supplied continuously throughout the differentiation into cardiac organoids in order to mimic the continuous drug exposure during fetal development. Samples were terminated on Day 20 for motion tracking analysis and for fluorescence/confocal imaging to assess the developmental toxicity of specific drugs based on the organoid morphology and contractile physiology.

Analysis of contraction physiology

Organoids were imaged in an onstage microscope incubator (OkoLab Stage Top Incubator, UNO-T-H-CO2) at 37 ˚C and 5% CO2 to maintain standard physiological conditions on a Nikon Ti-E inverted microscope with Andor Zyla 4.2+ digital CMOS camera. Videos of contracting cardiac organoids were recorded at 50 frames per second for ten seconds in brightfield and exported as a series of single frame image files. Contraction physiology was assessed using video-based motion tracking software (Huebsch et al., 2015) that computes motion vectors based on block matching of pixel macroblocks from one frame to the next. The motion vectors were assimilated into a contraction motion waveform representative of contractile physiology, providing metrics such as contraction amplitude and frequency. Peak-to-peak interval is the time interval between contraction peak and relaxation peak.

Contraction physiology was also assessed by recording the calcium transient using GCaMP6f hiPSC-derived cardiac organoids. Videos were taken under GFP excitation at 40 ms exposure time with 25 frames per second. Calcium flux signals were exported as Z-axis profiles in ImageJ. The fluorescence bleaching decay was corrected and time decay parameters τ_0, τ_{50}, τ_{75} were computed using in-house MATLAB scripts. The pulse duration is the time interval at which the calcium flux is at the half of the maximum flux. The time interval τ_0 is defined as the time it takes for the calcium flux to reach peak fluorescence intensity, whereas τ_{50} and τ_{75} represent the time it takes for the calcium flux to decay 50% and 75% of the peak fluorescence, respectively.

Relationships within the functional data was visualized utilizing R. Normalization to the zero mean, or Z-normalization, was utilized to normalize and scale each parameter to have a mean of 0 with a range near 1. This preprocessing step ensures allows us to study the correlation and similarities of our studied variables. t-Stochastic Neighbor Embedding (t-SNE), an unsupervised machine learning algorithm, was used for exploratory data analysis of the impact of pattern sizes on the measured variables of the organoids. This modern dimensionality technique is able to take high-dimensional data and reduce multidimensional relationships between data to a lower dimensional space in such a way that similar relationships are grouped

nearer to one another with a higher probability than dissimilar relationships or objects. This is accomplished by first creating a probability distribution of higher dimensional objects such that more similar pairs of higher dimensional objects are given a higher probability with more dissimilar points given a lower probability. A second probability distribution is then generated from this probability distribution for a lower dimensional map in such a way that preserves the maximum amount of similarity between the two probability distributions. t-SNE's ability to capture linear and nonlinear relationships between many variables makes it a powerful and versatile tool for investigating complex patterns while preserving higher dimensional structure of our data. t-SNE plots were generated using suggested parameters for perplexity (van der Maaten and Hinton, 2008), in order to condense the relationships between multiple recorded parameters down to a two-dimensional representative plot. Measurements were collected from mean values collected from 166 organoids. The actual t-SNE analysis was performed in R utilizing Jesse Krijthe's 2015 package Rtsne: T-Distrubed Stochastic Neighbor Embedding using a Barnes-Hut Implementation (https://github.com/jkrijthe/Rtsne) to reduce the representation of our parameters to two dimensions. Pattern diameters were displayed by varying size and color of each point, and then individual parameters were investigated by applying a color gradient in the t-SNE plots. A heatmap of the same data was generated to visualize each variables impact with respect to pattern diameter concurrently (Gu et al., 2016), while a correlogram gives further insight into the impact between parameters (Wei et al., 2017) by utilizing Frank Harrell's Hmisc package to generate these figures https://CRAN.R-project.org/package=Hmisc.

Immunofluorescence staining and confocal microscopy

Organoids were characterized based on immunofluorescence staining patterns of cardiac tissue and smooth muscle-like tissue. After video recording, samples were sacrificed and fixed with 4% (vol/vol) paraformaldehyde (PFA) for 10 minutes. After PFA treatment, samples were washed and permeabilized with 0.2% (vol/vol) Triton X-100, blocked with 2% (wt/vol) bovine serum albumin (BSA) and incubated with the appropriate dilution of primary antibodies for 1 hour at room temperature. After incubation, the

primary antibody was removed and washed with PBS. Secondary fluorescent antibodies were then incubated in the dark for 2 hours at appropriate dilutions and nuclei were tagged with 300 nM DAPI. All primary and secondary antibodies used are listed in Supplemental Table 2. Confocal microscopy (Zeiss U880) was used to capture z-stacks (8 μm spacing between slices) of the organoids for height measurements and 3D reconstruction.

Morphological and structural characterization of cardiac organoids

The cardiac organoids were assessed based on three parameters that characterize the overall cardiac tissue distribution and 3D morphology (Supplemental Fig. 2). All images were imported into ImageJ for image reconstruction and analysis. The *Area Ratio* was measured by using the circular or elliptical tool to approximate the area of fluorescence of tissue staining positive for cardiac tissue, and normalizing this area relative to the area of the entire pattern. The *Height* was measured by locating the top and bottom of the organoids using confocal microscopy. Lastly, the *FWHM* was determined by measuring the tissue diameter at half of the organoid height.

Zebrafish whole embryo culture (zWEC) embryotoxicity assay

Transgenic *Tg(myl7:GFP)* zebrafish that express GFP exclusively in cardiomyocytes were used to observe myocardium development *in vivo* (Huang et al., 2003). Adult fish were bred to generate a few hundred synchronized embryos, which were divided into individual wells of approximately 50 embryos. The drug stocks were diluted in zebrafish embryo medium. Chemicals at the same concentrations described in Supplemental Table 1 were administered to chorionated zebrafish embryos within the first 5 hpf, which is the estimated equivalent to the time point when the chemicals are introduced to the human cardiac organoids. Fresh embryo medium with chemicals is replaced at 24 hpf, when the embryos have developed a prominent linear heart tube, but not yet undergone looping. At 48 hpf, cardiac morphology and looping were scored as the first assessment of cardiac developmental toxicity on *in vivo* organogenesis. zWEC embryotoxic potentials of each chemical were scored based on the percentage of embryos exhibiting distinct

cardiac morphology at 48 hpf. Normal looping (D-looping) refers to looping to the right-hand side of the embryo. Reverse looping (L-looping) is classified as looping towards the left side of the embryo, while no looping (N-looping) refers to a straight linear heart tube that has not successfully undergone cardiac looping events. A subset (~20%) of embryos, including controls, did not express the GFP transgene, potentially due to silencing, and therefore cannot be classified as D/L/N-looping in this assay. Treatments that produced a rate of GFP absence that was significantly higher than controls are considered to reflect a severe abnormality in myocardial development.

Statistical Analysis

Data was plotted as box plots or mean ± s.d. For single comparisons between two individual groups, a two-sided Student's t-test was used, and $p \leq 0.05$ was considered significant. For comparisons between more than two groups, one-way analysis of variance (ANOVA) was performed and $p \leq 0.05$ was considered significant. ANOVA analysis was supplemented with multiple comparison tests to determine significance between groups.

References

Gu, Z., Eils, R., and Schlesner, M. (2016). Complex heatmaps reveal patterns and correlations in multidimensional genomic data. Bioinformatics *32*, 2847–2849.

Hoang, P., Wang, J., Conklin, B.R., Healy, K.E., and Ma, Z. (2018). Generation of spatial-patterned early-developing cardiac organoids using human pluripotent stem cells. Nat. Protoc. *13*, 723–737.

Huang, C.J., Tu, C.T., Hsiao, C. Der, Hsieh, F.J., and Tsai, H.J. (2003). Germ-line transmission of a myocardium-specific GFP transgene reveals critical regulatory elements in the cardiac myosin light chain 2 promoter of zebrafish. Dev. Dyn. *228*, 30–40.

Huebsch, N., Loskill, P., Mandegar, M.A., Marks, N.C., Sheehan, A.S., Ma, Z., Mathur, A., Nguyen, T.N., Yoo, J.C., Judge, L.M., et al. (2015). Automated Video-Based Analysis of Contractility and Calcium Flux in Human-Induced Pluripotent Stem Cell-Derived Cardiomyocytes Cultured over Different Spatial Scales. Tissue Eng. Part C Methods *21*, 467–479.

Lian, X., Hsiao, C., Wilson, G., Zhu, K., Hazeltine, L.B., Azarin, S.M., Raval, K.K., Zhang, J., Kamp, T.J., and Palecek, S.P. (2012). Robust cardiomyocyte differentiation from human pluripotent stem cells via temporal modulation of canonical Wnt signaling. Proc. Natl. Acad. Sci. *109*, E1848–E1857.

Liu, W., Dong, W., Hoffman, E.J., Fernandez, T. V, and Gupta, A.R. (2019). CHD8 regulates the balance between proliferation and differentiation of human iPSCs in neural development. bioRxiv 732693.

van der Maaten, L., and Hinton, G. (2008). Visualizing Data using t-SNE. J. Mach. Learn. Res. *9*, 2579–2605.

Wei, T., Simko, V., Levy, M., Xie, Y., Jin, Y., and Zemla, J. (2017). Visualization of a Correlation Matrix. Statistician *56*, 316–324.